reactions

MDPI

Article

Fischer-Tropsch Synthesis: The Characterization and Testing of Pt-Co/SiO_2 Catalysts Prepared with Alternative Cobalt Precursors

Mohammad Mehrbod [1], Michela Martinelli [2], Caleb D. Watson [3], Donald C. Cronauer [4], A. Jeremy Kropf [4] and Gary Jacobs [1,3,*]

[1] Department of Mechanical Engineering, UTSA, One UTSA Circle, San Antonio, TX 78249, USA; m_mehrbod2000@yahoo.com
[2] Center for Applied Energy Research, University of Kentucky, 2540 Research Park Drive, Lexington, KY 40511, USA; michela.martinelli@uky.edu
[3] Department of Biomedical Engineering and Chemical Engineering, UTSA, One UTSA Circle, San Antonio, TX 78249, USA; caleb.watson378@gmail.com
[4] Argonne National Laboratory, Argonne, IL 60439, USA; dccronauer@anl.gov (D.C.C.); kropf@anl.gov (A.J.K.)
* Correspondence: gary.jacobs@utsa.edu; Tel.: +1-210-458-7080

Abstract: Different low-cost cobalt precursors (acetate, chloride) and thermal treatments (air calcination/H_2 reduction versus direct H_2-activation) were investigated to alter the interaction between cobalt and silica. H_2-activated catalysts prepared from cobalt chloride had large Co^0 particles (XRD, chemisorption) formed by weak interactions between cobalt chloride and silica (temperature programmed reduction (TPR), TPR with mass spectrometry (TPR-MS), TPR with extended X-ray absorption fine structure (EXAFS) and X-ray absorption near edge spectroscopy (XANES) techniques) and retained Cl-blocked active sites, resulting in poor activity. In contrast, unpromoted Co/SiO_2 catalysts derived from cobalt acetate had strong interactions between Co species and silica (TPR/TPR-MS, TPR-EXAFS/XANES); adding Pt increased the extent of the Co reduction. For these Pt-promoted catalysts, the reduction of uncalcined catalysts was faster, resulting in larger Co^0 clusters (19.5 nm) in comparison with the air-calcined/H_2-activated catalyst (7.8 nm). Both catalysts had CO conversions 25% higher than that of the Pt-promoted catalyst prepared in the traditional manner (air calcination/H_2 reduction using cobalt nitrate) and three times higher than that of the traditional unpromoted Co/silica catalyst. The retention of residual cobalt carbide (observed in XANES) from cobalt acetate decomposition impacted performance, resulting in a higher C_1–C_4 selectivity (32.2% for air-calcined and 38.7% for uncalcined) than that of traditional catalysts (17.5–18.6%). The residual carbide also lowered the α-value and olefin/paraffin ratio. Future work will focus on improving selectivity through oxidation–reduction cycles.

Keywords: Fischer-Tropsch synthesis; cobalt; silica; cobalt acetate; cobalt chloride; platinum; promoters; direct reduction; TPR-XANES; TPR-EXAFS; TPR-MS

check for updates

Citation: Mehrbod, M.; Martinelli, M.; Watson, C.D.; Cronauer, D.C.; Kropf, A.J.; Jacobs, G. Fischer-Tropsch Synthesis: The Characterization and Testing of Pt-Co/SiO_2 Catalysts Prepared with Alternative Cobalt Precursors. *Reactions* **2021**, *2*, 129–160. https://doi.org/10.3390/reactions2020011

Academic Editors: Ajay K. Dalai and Dmitry Yu. Murzin

Received: 20 April 2021
Accepted: 27 May 2021
Published: 1 June 2021

Publisher's Note: MDPI stays neutral with regard to jurisdictional claims in published maps and institutional affiliations.

Copyright: © 2021 by the authors. Licensee MDPI, Basel, Switzerland. This article is an open access article distributed under the terms and conditions of the Creative Commons Attribution (CC BY) license (https://creativecommons.org/licenses/by/4.0/).

1. Introduction

Fischer-Tropsch synthesis (FTS) is a heterogeneously catalyzed reaction used to produce high-value synthetic hydrocarbons, which are further upgraded to produce transportation fuels and chemicals from fossil and renewable sources [1]. Iron (Fe), cobalt (Co), and ruthenium (Ru) are three well-known metals that serve as active catalysts in FTS. Co and Ru have a low intrinsic water-gas shift activity, so they are the most suitable active metals for converting natural gas-derived syngas, which has a high H_2/CO ratio. From the standpoint of economics, Co is more practical because it is less expensive and more abundant than Ru.

Nevertheless, because Co is far more expensive than Fe the efficient use of cobalt involves maximizing the CO conversion on a per gram of catalyst basis, as well as the

C_{5+} selectivity of products formed from the FTS reaction. To disperse cobalt as cobalt nanoparticles, conventional cobalt catalysts are prepared from the aqueous impregnation of cobalt nitrate, followed by drying, air calcination, and H_2 reduction [2]. Iglesia [3] showed that for typical FTS catalyst formulations, CO conversion is linked to the surface Co^0 active site density, indicating that the active sites of cobalt-based FTS catalysts are surface Co^0 atoms. Improving CO conversion on a per gram of catalyst basis requires the development of catalysts with higher surface Co^0 active site densities [3,4]. In conventional Co-based FTS catalysts, the Co^0 active site density is typically improved by decreasing the Co^0 particle size and increasing the extent of the reduction of cobalt oxides prepared from the calcination of cobalt nitrate particles. The resulting average size of Co^0 clusters following the activation of the catalyst in H_2 depends on the interaction between cobalt oxide species and the support. Stronger interactions between the support and cobalt oxides, such as those observed with 39 catalysts [4,5], result in a smaller average Co^0 nanoparticle size following H_2 activation but a lower extent of reduction. To increase the extent of reduction, promoters such as Pt, Re, and Ru are used [3–15]. If the Co particles are too small (e.g., <2–4 nm), however, they are susceptible to deactivation phenomena, including oxidation and cobalt-support compound formation [16–21].

In contrast to Co/Al_2O_3, very weak interactions exist between Co oxide and SiO_2 prepared from the air calcination of cobalt nitrate, and cobalt tends to agglomerate into larger clusters. This has led to researchers exploring alternative preparation methods to improve the dispersion. For example, Bambal et al. [22] added chelating agents such as nitrilotriacetic acid and ethylenediaminetetraacetic acid to silica, which modified the surface prior to adding cobalt nitrate; the resulting dispersions were improved by 2–4.3 times. Another example was the use of atomic layer deposition (ALD), which enabled a decrease in the size of Co particles from 10.1 nm to the range of 5.6–5.9 nm for Co/silica catalysts with Co loadings in the range of 20–25% [23].

While researchers have primarily used cobalt nitrate $Co(NO_3)_2{\cdot}6H_2O$ as the cobalt precursor and investigated catalysts prepared with different supports, promoter metals, and activation procedures, alternative cobalt precursors such as cobalt chloride and cobalt acetate have been examined to a lesser degree. Bae et al. [24] applied these three precursors to produce $Co/AlPO_4$ through impregnation methods. The results show that the catalyst prepared with cobalt nitrate exhibited a higher CO conversion and C_{8+} selectivity in comparison with the others.

With alternative precursors, the typical treatment of the catalyst involves the calcination of the dispersed cobalt salt in air flow and then the H_2 reduction of cobalt oxides. Studies using mesoporous MCM-41 as the support revealed that applying organic precursors (e.g., cobalt acetate or cobalt acetylacetonate) instead of inorganic ones (e.g., cobalt nitrate or cobalt chloride) resulted in very small cobalt particles being uniformly distributed throughout the mesoporous MCM-41 support [25]. On the other hand, very large cobalt particles were found to form on Co/MCM-41 prepared from cobalt chloride. This result indicates that exploring different cobalt compounds may help to optimize cobalt dispersion to maximize the cobalt active site density. However, as this study reveals, the precursors used may strongly interact with the support, facilitating cobalt-support compound formation or, at the other end of the spectrum, interact weakly with the support to promote cobalt agglomeration during pretreatment and reduction steps. Both scenarios tend to lower the CO hydrogenation activity.

Sun et al. [26] observed a higher catalyst activity due to higher dispersions of cobalt metal caused by the co-impregnation of a mixture of cobalt (II) nitrate and cobalt (II) acetate (containing 10 wt.% Co: 5 wt.% from cobalt nitrate and 5 wt.% from cobalt acetate) on SiO_2 as compared to the catalyst prepared from the mono-precursor and using mild process conditions (1 MPa, 513 K, and $H_2/CO = 2$). Thereafter, the catalyst activity and extent of reduction of cobalt oxide were remarkably increased by adding small amounts of reductive promoters such as Ru, Pt, and Pd (weight ratio of promoter to Co was 1/50) through co-impregnation [27].

Additionally, the effects of pretreatment conditions and cobalt precursors on the resulting Co clusters that formed in SiO_2-supported catalysts were investigated. The catalysts were prepared through the aqueous impregnation of SiO_2 with a solution of cobalt acetate or cobalt nitrate, followed by air calcination and a reduction in hydrogen. The endothermicity of cobalt nitrate decomposition favored Co_3O_4 crystallite formation, whereas the exothermicity of cobalt acetate decomposition led to barely reducible cobalt silicate [28].

Foregoing calcination and using direct reduction of cobalt nitrate on silica oxide were investigated in the early 2000s, and the new treatment method obtained resulted in stronger interactions between cobalt oxides and supports and a smaller cobalt particle size [29,30]. Although some improvements in CO conversion and active site density were observed, a significant fraction of cobalt oxide remained inaccessible and unreduced. Later, Wigzell et al. [31] and Martinelli et al. [32] reported on the phenomena occurring during the direct decomposition/reduction of cobalt nitrate on silica support. The observations were losses of water by dehydration, the thermal decomposition of cobalt nitrate, the reductive decomposition of cobalt nitrate with the evolution of NO, the exothermic oxidation of CoO_x to Co_3O_4 spinel by NO_X, the reduction of Co_3O_4 spinel to CoO, and finally the reduction of CoO to cobalt metal.

On the other hand, moderate and strong interactions were observed with Co/TiO_2 and Co/Al_2O_3. Our recent studies have shown significant improvements in CO conversion and product selectivity for Co/SiO_2 when using the combination of direct reduction of cobalt nitrate and the incorporation of reduction promoters such as Pt and Re [32]. Compared using the same space velocity, Re- and Pt-promoted 12% Co/SiO_2 catalysts activated by the direct H_2 reduction of cobalt nitrate had initial conversions in a CSTR that were up to 3.8 times higher and 71% higher than H_2-activated unpromoted and Pt-promoted air-calcined catalysts, respectively. The methane selectivity was lower (6.8 and 8.0% for Re- and Pt-promoted catalysts, respectively, by the direct H_2 reduction of cobalt nitrate versus 12.5 and 10.1% for H_2-activated unpromoted and Pt-promoted air-calcined catalysts) and the C_{5+} selectivity was higher (81.2 and 81.5% for Re- and Pt-promoted catalysts, respectively, by the direct H_2 reduction of cobalt nitrate versus 73.4 and 78.8% for H_2-activated unpromoted and Pt-promoted air-calcined catalysts). On the other hand, this method did not have as dramatic of an effect on improving cobalt particle size and CO conversion for more strongly interacting Co/TiO_2 and Co/Al_2O_3 [33,34] catalysts, where the support already stabilizes small Co particles.

According to the Millipore Sigma website, the cost of 100 g of cobalt (II) nitrate hexahydrate $Co(NO_3)_2{\cdot}6H_2O$ is almost 700% more than that of the same amount of cobalt (II) acetate tetrahydrate $(CH_3COO)_2Co{\cdot}4H_2O$ and about 1050% more expensive than cobalt (II) chloride hexahydrate $CoCl_2{\cdot}6H_2O$ [35]. Therefore, it would be beneficial if less expensive salts could be substituted in place of cobalt nitrate to prepare FTS catalysts.

In this paper, we investigate the utilization of alternative cobalt compounds such as cobalt (II) acetate and cobalt (II) chloride using SiO_2 as the support. Both unpromoted and Pt-promoted catalysts are investigated, and the direct H_2 reduction of the cobalt compounds versus air calcination/H_2 reduction is also explored. The working hypothesis is that alternative cobalt compounds, as well as the cobalt oxides derived from their calcination, should have interactions with SiO_2 significantly different from those observed in conventional Co/SiO_2 catalysts derived from cobalt nitrate and using air calcination/H_2 reduction treatments. The objectives of the work are to confirm this hypothesis and show that these differences could be applied to, in some cases, favorably alter the properties of the catalyst (e.g., cobalt size, reducibility, and active site density) and in turn influence the performance parameters (e.g., activity, selectivity, and/or stability) of cobalt catalysts for GTL. To better understand the decomposition reactions occurring with each precursor, synchrotron methods such as temperature-programmed extended X-ray absorption fine-structure spectroscopy (TPR-EXAFS) and temperature-programmed X-ray absorption near-edge spectroscopy (TPR-XANES) were employed, as well as TPR with mass spectrometry

(TPR-MS). These results provide new insight into the reasons behind the observed activity and selectivity of catalysts prepared from alternative cobalt precursors and also shed light on future research directions.

2. Materials and Methods

2.1. Catalyst Preparation

A total of 12 wt.% Co/SiO_2 catalysts were prepared using incipient wetness impregnation (IWI) of aqueous solutions of either cobalt (II) acetate tetrahydrate ($Co(CH_3COO)_2{\cdot}4H_2O$) (Alfa Aesar, Tewksbury, MA, USA) or cobalt (II) chloride hexahydrate ($CoCl_2{\cdot}6H_2O$) (Alfa Aesar, Tewksbury, MA, USA) and PQ SiO_2 (PQ Corp., CS-2133, Malvern, PA, USA) as the support, where the aqueous solution was added to fill the pores of the support. The solubility of cobalt acetate tetrahydrate in water is 380 g/L at 20 °C, and that of cobalt chloride hexahydrate in water is 529 g/L at 20 °C. The specific volume of the pores is high for silica, at 2.68 mL/g [36]. In our work, two impregnation steps with intermittent vacuum drying steps were used to load the salts. Following each impregnation step, water from the pores of the catalysts was evaporated out using a Heidolph (Schwabach, Germany) rotary evaporator unit with the temperature increasing slowly from 80 to 100 °C. Afterward, multiple batches were formed by dividing each parent batch, with half being allocated to prepare Pt-promoted catalysts and half being set aside for the unpromoted catalyst. In order to prepare a 0.5 wt.% Pt-promoted catalyst, the cobalt precursor was added using IWI and then the catalyst was dried again using the rotary evaporator unit. The unpromoted and Pt-promoted portions were further divided in half, such that one half was calcined in flowing air for 4 h at 350 °C and one half remained uncalcined. Weight percentages are reported assuming a calcined catalyst basis.

2.2. BET Surface Area and Porosity Measurements

The BET surface area and porosity characteristics were measured using a Micromeritics 3-Flex system. Before performing the test, the temperature was gradually ramped up to 160 °C and the sample was evacuated for at least 12 h to approximately 50 mTorr. This procedure was followed for calcined, uncalcined/reduced, calcined/reduced catalysts; on the other hand, the uncalcined catalysts were evacuated at room temperature. The BJH method was also used to determine the pore volume and average pore diameter, as well as the pore size distribution as a function of pore radius using the relation dV/d (log D).

2.3. X-Ray Diffraction

X-ray diffraction (XRD) was carried out using a Rigaku Ultima IV diffractometer (RIGAKU, Tokyo, Japan) equipped with a dual-position graphite diffracted beam monochromator for Cu using Cu Kα radiation at 43 kV and 30 mA. Prior to XRD characterization, samples were reduced in hydrogen (American Welding & Gas, Lexington, KY, USA) for 18 h at 350 °C, cooled to 20 °C, and then passivated with 1% O_2 in nitrogen (American Welding & Gas, Lexington, KY, USA). The parameters used were a 2θ range of 5–80°, a scan rate of 0.01° per step, and a scan time of 4 s per step. The integral breadth method was used to calculate the average domain size using WinFit 1.2 [37].

2.4. Temperature-Programmed Reduction (TPR) and TPR-MS

The TPR profiles of uncalcined and calcined catalysts were recorded using an Altamira AMI-300R (Pittsburgh, PA, USA) unit equipped with a thermal conductivity detector (TCD). Calcined catalysts were first pretreated in flowing helium at 30 cm^3/min at 300 °C (1 °C/min heating rate) for 1 h and cooled. Uncalcined catalysts were treated in 30 cm^3/min helium at room temperature for 1 h. The TPR was performed using a 10% H_2/Ar gas mixture referenced to argon at a flow rate of 30 cm^3/min. Each sample was heated from 50 to 1000 °C using a heating ramp of 10 °C/min. The gaseous products of decomposition/reduction were analyzed using an on-line quadrupole mass spectrometer (Hiden, Warrington, UK). Appropriate mass-to-charge ratios (m/z) examined, including

those in the cracking patterns, were 2, 1 for H_2; 18, 17, 16 for H_2O; 44, 43, 29, 15 for C_2H_4O; 16, 15, 14 for CH_4; 44, 28, 16 for CO_2; and 28, 16, 12 for CO.

2.5. Hydrogen Chemisorption and Percentage Reduction by Pulse Reoxidation

Hydrogen chemisorption was conducted using temperature-programmed desorption (TPD) and measured with the Altamira AMI-300R instrument (Pittsburgh, PA, USA). Each catalyst was loaded into a quartz reactor tube and activated in situ in a flow of 10 cm^3/min of H_2 mixed with 20 cm^3/min of argon at 350 °C for 10 h prior to cooling under flowing H_2 to 100 °C. The sample was held at 100 °C under flowing Ar to remove and/or prevent the adsorption of weakly bound species prior to increasing the temperature slowly to 350 °C, the activation temperature of the catalyst. The catalyst was held under flowing Ar to desorb any remaining chemisorbed hydrogen until the TCD signal returned to the baseline. The TPD spectrum was integrated and the number of moles of desorbed H_2 was determined by comparing its desorption profile area to the areas of calibrated hydrogen pulses. Dispersion calculations were based on the assumption of a 1:1 H:Co stoichiometric ratio and a spherical cobalt cluster morphology. After the TPD of hydrogen, the sample was reoxidized at 350 °C using pulses of O_2. The percentage of reduction was calculated by assuming that the metallic Co^0 reoxidized to Co_3O_4.

2.6. TPR-EXAFS/TPR-XANES Spectroscopies

In situ H_2-TPR XAFS studies were performed at the Materials Research Collaborative Access Team (MR-CAT) beamline at the Advanced Photon Source, Argonne National Laboratory. A cryogenically cooled Si (1 1 1) monochromator selected the incident energy and a rhodium-coated mirror rejected higher-order harmonics of the fundamental beam energy. The experiment setup was similar to that outlined by Jacoby [38]. A stainless steel multi-sample holder (3.0 mm i.d. channels) was used to monitor the in situ reduction of 6 samples during a single TPR run. Approximately 6 mg of each sample was loaded as a self-supporting wafer in each channel. The catalyst to diluent (ground silica) weight was approximately 1:1. The holder was placed in the center of a quartz tube equipped with gas and thermocouple ports and Kapton windows. The amount of sample used was optimized for the Co K-edge, considering the absorption of the support by Si. The quartz tube was placed in a clamshell furnace mounted on the positioning table. Each sample cell was positioned relative to the beam by finely adjusting the position of the table to an accuracy of 20 μm (for repeated scans). Once the sample positions were fine-tuned, the reactor was purged with He for more than 5 min at 100 mL/min, then the reactant gas (H_2/He, 3.5%) was flowed through the samples (100 mL/min) and a temperature ramp of ~1.0 °C/min was initiated for the furnace to 600 °C. The Co K-edge spectra were recorded in transmission mode and a Co metallic foil spectrum was measured simultaneously with each sample spectrum for energy calibration. X-ray absorption spectra for each sample were collected from 7528 to 8503 eV.

The data reduction of the EXAFS/XANES spectra was carried out using the WinXAS program [39]. The details of the XANES and EXAFS analyses are provided in the appendices of our previous article and will not be repeated here for the sake of brevity [40]. EXAFS data reduction and fitting were carried out using the catalysts in their final state following TPR and cooling in flowing H_2 using the WinXAS [39], atoms [41], FEFF [42], and FEFFIT [42] programs. The k-range used for the fittings was 3–10 $Å^{-1}$. Fitting was confined to the first Co-Co metallic coordination shell.

2.7. Catalytic Activity

FTS reaction tests were conducted using a 1 L continuously stirred tank reactor (CSTR) equipped with a magnetically driven stirrer with a turbine impeller, a gas-inlet line, and a vapor outlet line with a stainless steel (SS) fritted filter (7 μm) placed external to the reactor. A tube fitted with a SS fritted filter (2 μm opening) extended below the liquid level of the reactor for withdrawing reactor wax to maintain a nearly constant liquid level in the reactor.

Separate mass flow controllers were used to control the flows of H_2 and CO at the desired flow rates. The reactant gases were premixed in a vessel before entering the reactor. CO was passed through a vessel containing lead oxide-alumina to remove traces of iron carbonyls. The mixed gases entered the CSTR below the stirrer, which was operated at 750 rpm. The reactor slurry temperature was maintained constant by a temperature controller.

Prior to performing the reaction test, the catalyst (about 10 g on a cobalt oxide basis) was loaded into a fixed-bed reactor for ex situ reduction at 350 °C under atmospheric pressure for 18 h using a gas mixture of H_2/He (120 L(STP)/h) with a molar ratio of 1:3. The reduced catalyst was then transferred to a 1 L CSTR, which contained 310 g of melted Polywax 3000, by pneumatic transfer under the protection of N_2 gas. Weighing the reactor before and after the transfer of catalyst ensured that all catalyst powder was successfully transferred to the reactor. The transferred catalyst was further reduced in situ at 230 °C at atmospheric pressure using pure H_2 (30 L(STP)/h) for an additional 12 h before starting the FTS reaction.

In this study, catalytic tests were performed at the following process conditions: T = 220 °C, P = 20 atm, H_2/CO = 2 mol/mol, SV = 6 slph/g_{cat}. The reactant gas mixture was analyzed prior to sending to the reactor to check its composition. The reaction products were continuously removed from the vapor space of the reactor and passed through two traps: a warm trap maintained at 100 °C and a cold trap held at 0 °C. The uncondensed vapor stream was reduced to atmospheric pressure. The gas flow was measured using a wet test meter and analyzed by online micro-GC (Inficon-MicroGC Fusion, Bad Ragaz, Switzerland). The accumulated reactor liquid products were removed every 24 h by passing through a 2 μm sintered metal filter located below the liquid level in the CSTR. The reaction products were collected in three traps maintained at different temperatures: a hot trap (200 °C), a warm trap (100 °C), and a cold trap (0 °C). The products were separated into different fractions (rewax, wax, oil, and aqueous) for quantification. However, oil and wax fractions were mixed prior to GC analysis (Agilent, Santa Clara, CA, USA).

3. Results and Discussion

3.1. Morphological and Structural Properties

Table 1 lists the BET surface area, pore volume, and average pore diameter considering the N_2 adsorption branch for the catalysts prepared using cobalt acetate and cobalt chloride precursors on SiO_2, while Figure 1 shows their pore size distributions (PSD). Considering that silica has a surface area of 349 m^2/g (Table 1), the addition of 12.3 wt.% Co metal was equivalent to 16.75 wt.% Co_3O_4, 51.9 wt.% cobalt acetate tetrahydrate, and 49.7% cobalt (II) chloride hexahydrate. Thus, assuming that there is no pore blocking, the surface area should decrease to 293 m^2/g for the calcined catalysts, 169.3 m^2/g for uncalcined cobalt acetate catalyst, and 177.1 m^2/g for the uncalcined cobalt (II) chloride hexahydrate catalyst. The air-calcined unpromoted and Pt-promoted catalysts had surface areas of 242–257 m^2/g, suggesting that some minor pore blocking occurred. The uncalcined unpromoted and Pt-promoted cobalt acetate/silica catalysts had surface areas in the range of 148–160 m^2/g, also indicating that minor pore blocking by the cobalt salt took place. Finally, the cobalt chloride/silica catalysts had surface areas in the range of 192–207 m^2/g, suggesting that no significant pore blocking by the cobalt chloride precursor took place. After the reduction, assuming that no pore blocking by Co^0 took place, the surface area should be 308.7 m^2/g. The surface areas for reduced catalysts followed this trend: cobalt chloride air-calcined/reduced (average ~285 m^2/g)~cobalt chloride direct reduction (average ~276 m^2/g) > cobalt acetate direct reduction (average ~265 m^2/g) > cobalt acetate air-calcined/reduced (average ~248 m^2/g). Thus, while minor pore blocking occurred for all cobalt chloride-derived catalysts, the extent of pore blocking was slightly higher for cobalt acetate-derived catalysts, especially with air calcination. The average pore diameter (adsorption branch) was similar for most catalysts (~16.2–19.7 nm), as shown in Table 1. However, the unpromoted uncalcined cobalt chloride catalysts had larger average pore diameters of 21.1 nm, suggesting the preferential filling of narrower

pores by the precursor. The treatment of this catalyst tended to increase the pore diameter slightly (22.2 nm, 22.6 nm, and 24.3 nm for direct H_2 reduction, air calcination, and air calcination/H_2 reduction, respectively).

Table 1. BET surface area and BJH porosity measurement (N_2 adsorption branch).

Sample	Thermal Treatment	A_s (BET) (m^2/g)	V_p (BJH Ads) (cm^3/g)	Average D_p (BJH Ads) (nm)
SiO_2	Air-calcined	349	2.64	35.1
12% Co/SiO_2 from cobalt acetate	Uncalcined	160	0.64	16.2
	Reduced	256	1.01	16.4
	Air-calcined	244	1.09	19.3
	Air-calcined/reduced	247	1.10	19.2
0.5% Pt-12% Co/SiO_2 from cobalt acetate	Uncalcined	148	0.59	16.2
	Reduced	273	1.15	17.8
	Air-calcined	242	1.05	18.5
	Air-calcined/reduced	248	1.08	18.8
12% Co/SiO_2 from cobalt chloride	Uncalcined	207	0.91	21.1
	Reduced	287	1.43	22.2
	Air-calcined	250	1.28	22.6
	Air-calcined/reduced	285	1.57	24.3
0.5% Pt-12% Co/SiO_2 from cobalt chloride	Uncalcined	192	0.87	19.6
	Reduced	265	1.07	17.6
	Air-calcined	257	1.12	19.2
	Air-calcined/reduced	284	1.29	19.7

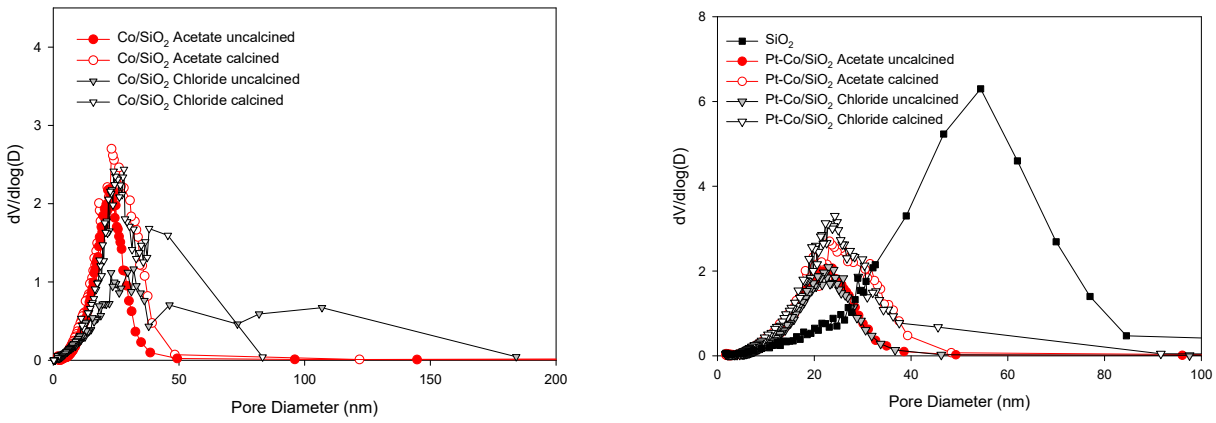

Figure 1. Pore size distribution (PSD, adsorption branch) for unpromoted and Pt-promoted Co/SiO_2 prepared from cobalt acetate and cobalt chloride, including by direct H_2 reduction versus air calcination/H_2 reduction.

Figure 2 shows the XRD patterns of the precursors prior to activation. Uncalcined cobalt acetate catalysts (Figure 2c,d, top left) had a complex series of peaks at 12.9°, 18.6°, 21°, 22°, 23.2°, 24.8°, 28.3°, 30.9°, and 44.7° for cobalt acetate crystallites. Following calcination (Figure 2a,b, top left-), peaks for Co_3O_4 emerged at 31° (220), 36.8° (311), 44.7° (400), 59.2° (511), and 65.1° (440). Interestingly, no XRD peaks were detected for the uncalcined cobalt chloride catalysts, suggesting that no significant long-range order exists for supported cobalt chloride crystallites (Figure 2g,h, top right-). Following calcination (Figure 2e,f, top right), a wide spectrum of peaks emerged, with peaks at 16°, 20.7°, 31.2°, 33°, 37.7°, 39.4°, and 42.2°. These peaks were generally in good agreement with Co_2SiO_4, suggesting that a minor fraction of cobalt chloride converted to a spinel structure of the form AB_2X_4. This suggests strong interactions between these species and the silica support, in agreement with the broad features in the high-temperature region of the TPR profiles. Note, however, that the majority of Co in the calcined cobalt chloride catalysts was reduced in a similar manner to the uncalcined cobalt chloride catalysts, suggesting that the majority

of cobalt remained in chloride form. The color of the catalyst remained pink even after air calcination, indicating that the majority of the cobalt was present as cobalt chloride, rather than as Co_2SiO_4. This was confirmed in the TPR-EXAFS/XANES analyses, which need to be discussed. Therefore, the cobalt chloride following air calcination was amorphous and unable to be detected by XRD. After the H_2 reduction and passivation (Figure 2a–h, bottom), Co metal particles emerged that were primarily HCP for all catalysts, as peaks emerged at 41.5° (100); 44.5° (002); 47.4° (101); and, in some cases (Figure 2f,g, bottom), 62.7° (102) and (Figure 2c–h, bottom) 75.8° (110). Note that FCC has peaks such as 44.2° (111) and 75.9° (220) that are close to those of HCP; its presence cannot be ruled out, although a peak for 51.5° for (200) was not detected.

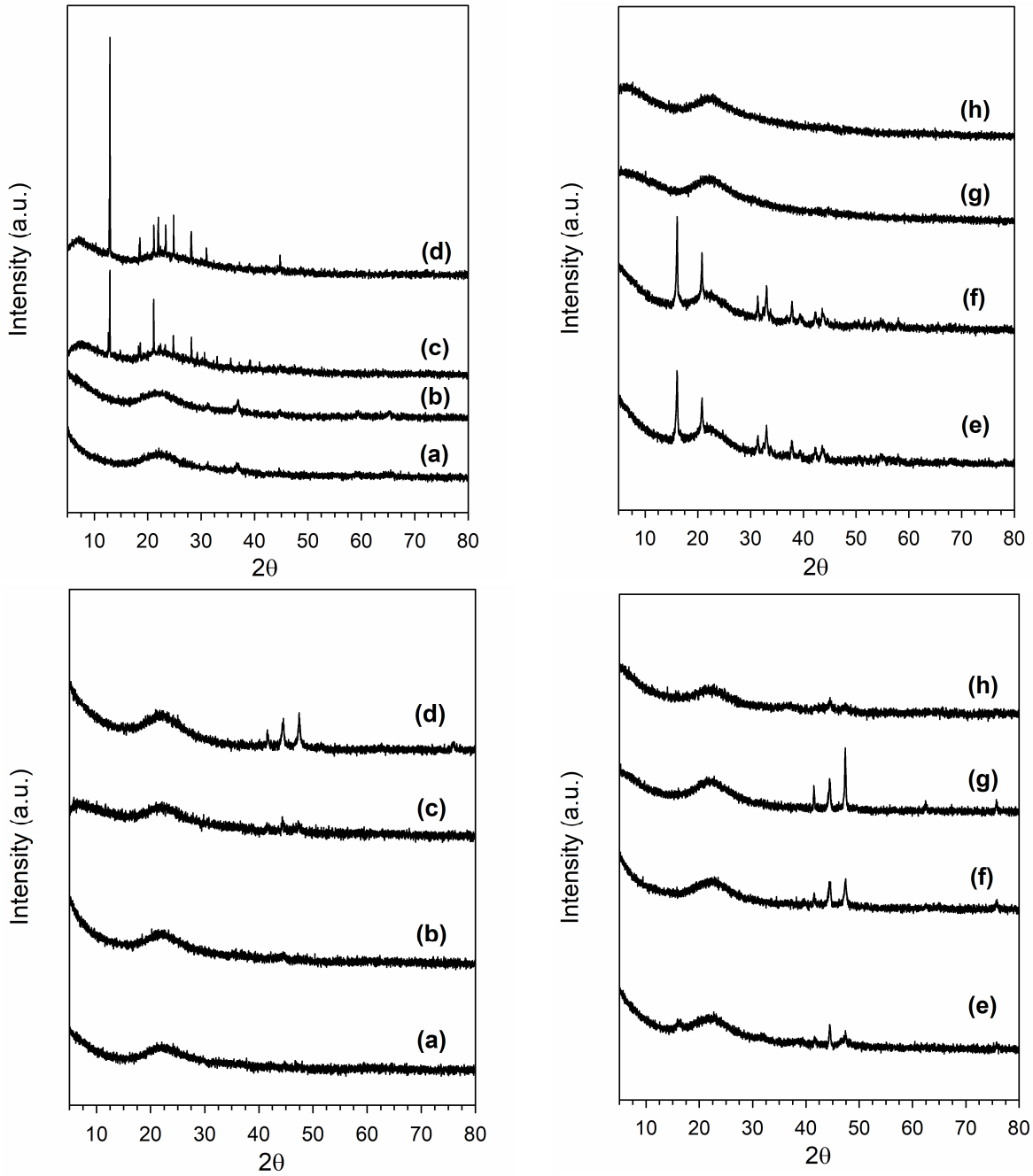

Figure 2. (**top left**) Co acetate precursor, (**top right**) Co chloride precursor, (**bottom left**) Co acetate catalyst after H_2 activation/passivation, (**bottom right**) Co chloride catalyst after H_2 activation/passivation for (**a**,**e**) air-calcined, (**b**,**f**) Pt-promoted and air-calcined, (**c**,**g**) uncalcined, (**d**,**h**) Pt-promoted, and uncalcined groups.

3.2. Cobalt Reducibility and Particle Size

Comparing the TPR, TPR-MS, TPR-EXAFS/XANES profiles, EXAFS fittings, and hydrogen chemisorption results, a picture emerges for each series of catalysts investigated. Starting with the 12% Co/SiO_2 catalysts prepared with cobalt acetate tetrahydrate, TPR profiles in Figure 3a are broad, with multiple peaks observed for unpromoted and 0.5% Pt-promoted calcined catalysts. The main peaks are situated at 340 °C and 680 °C.

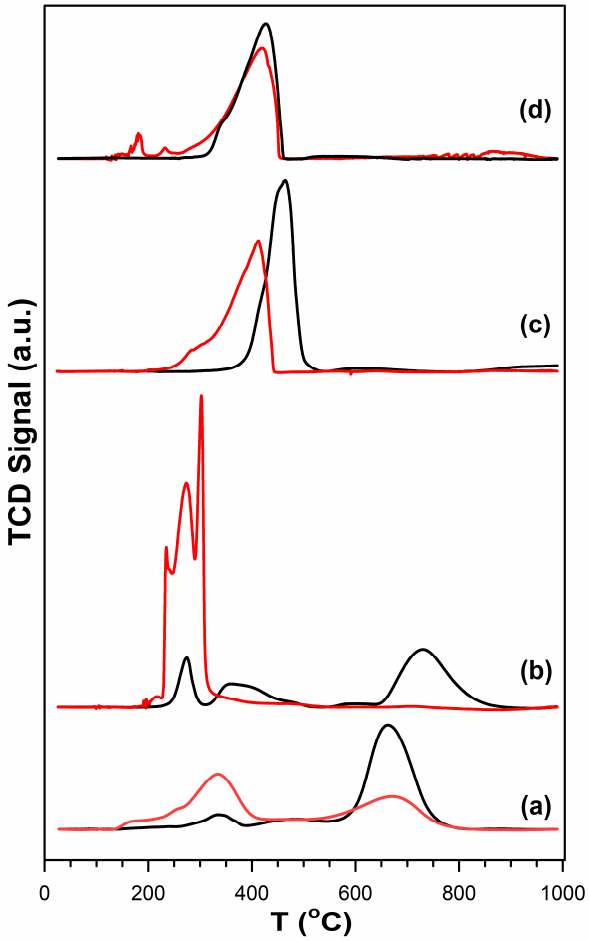

Figure 3. TPR profiles of (**a**,**c**) calcined and (**b**,**d**) uncalcined 12% Co/SiO_2 catalysts prepared with (**a**,**b**) cobalt acetate and (**c**,**d**) cobalt chloride, including (black) unpromoted and (red) 0.5% Pt-promoted catalysts.

Adding Pt significantly diminishes the high-temperature reduction peak and increases the low-temperature one. H_2 uptakes and H_2O evolution are confirmed for these catalysts in the TPR-MS profiles provided in Figure 4a,b. The H_2 evolution peaks are mirror images of the TCD signals. H_2O signals were observed to evolve at temperatures higher than those of H_2, indicating readsorption and desorption behavior as it interacts with the catalyst surface.

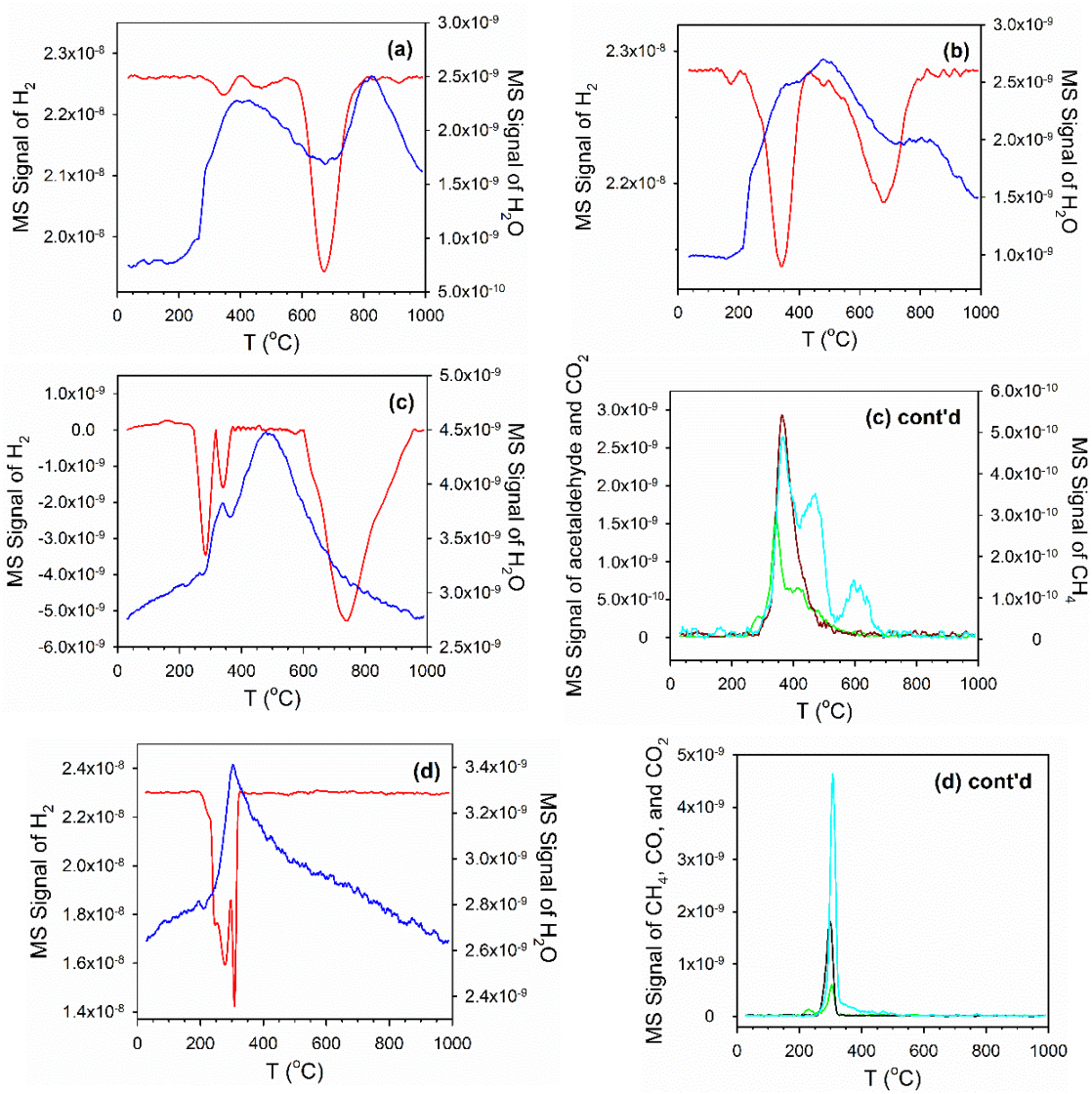

Figure 4. H_2-TPR profiles with the mass spectra analysis of the exhaust gas for 12% Co/SiO_2 catalysts prepared with cobalt acetate, including (**a**) calcined, (**b**) calcined promoted with 0.5% Pt, (**c**) uncalcined, and (**d**) uncalcined promoted with 0.5% Pt. (red), H_2 (blue), H_2O, (dark red), C_2H_4O (cyan), CH_4 (green), CO_2, and (black) CO.

TPR-EXAFS/XANES experiments were conducted for the catalysts prepared from cobalt acetate and the results are summarized in Figures 5–10. For the unpromoted calcined catalyst, the TPR-XANES spectra in Figure 5a and XANES snapshot spectra in Figure 6(a1) show that the initial catalyst contained a spinel oxide contribution consistent with Co_3O_4, as there is a second white line peak at 7.729 keV consistent with a fraction of Co^{3+}. By 300 °C, the contribution from the spinel has disappeared and only a peak for Co^{2+} remains, as shown in the first green spectrum of Figures 5a and 6(b1), consistent with CoO formation and a two-step reduction process of $Co_3O_4 + H_2 \rightarrow 3CoO + H_2O$ followed by $3CoO + 3H_2 \rightarrow 3Co^0 + 3H_2O$. The final green spectrum of Figure 5a indicates that reduction to Co^0 is nearly complete by 560 °C, which is Δ150 °C higher than the final temperature of 410 °C typical of the 12% Co/SiO_2 prepared by the traditional method using cobalt nitrate and with air calcination/H_2 reduction [32]. Figure 6(d1) shows that the final TPR-XANES spectrum at 600 °C resembles that of the Co^0 foil. This result suggests the presence of smaller, more interacting, cobalt oxide species in the catalyst derived from cobalt acetate and using air calcination prior to H_2 reduction.

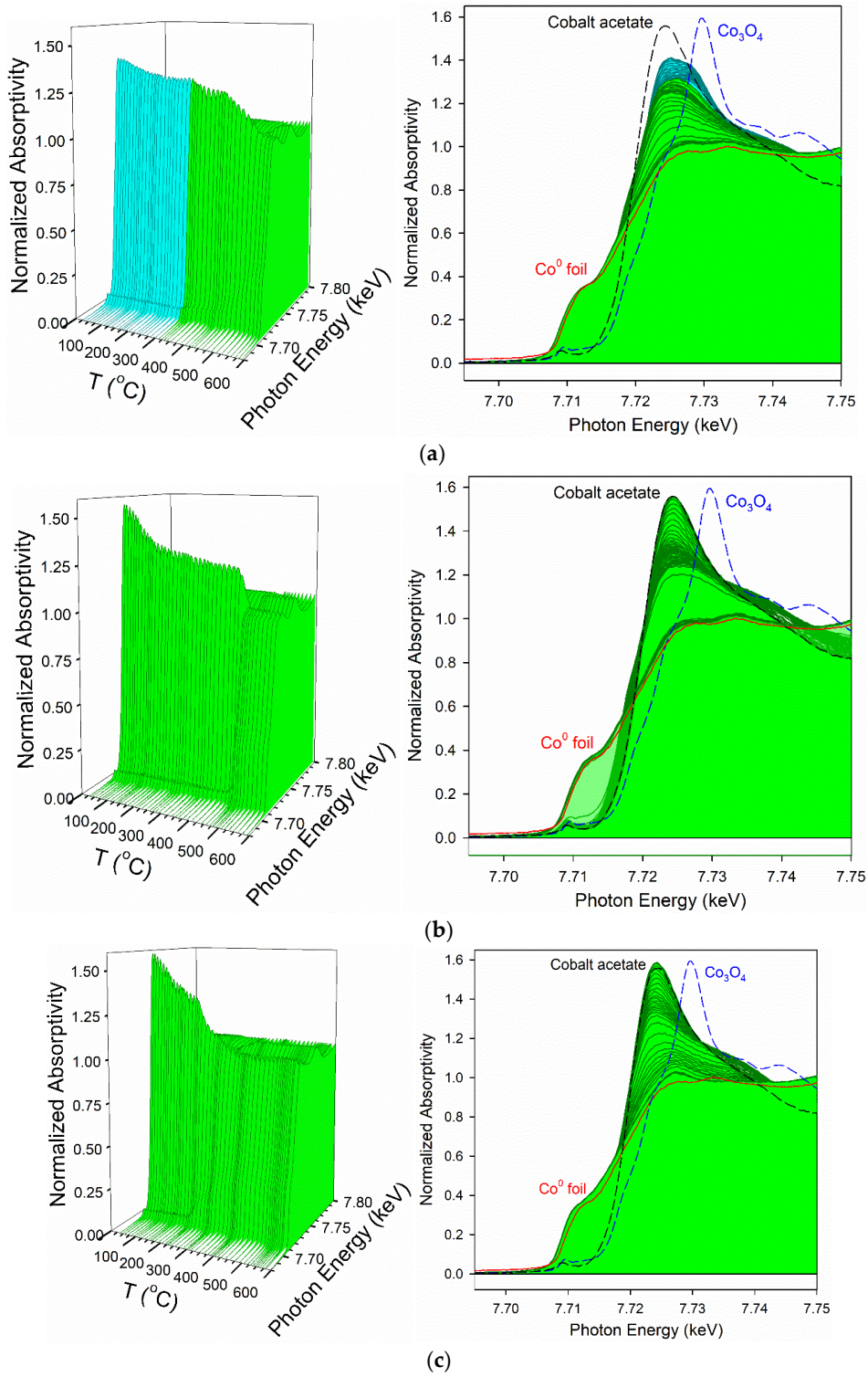

Figure 5. TPR-XANES profiles of (**a**) calcined 12% Co/SiO_2 from cobalt acetate, (**b**) uncalcined 12% Co/SiO_2 from cobalt acetate, and (**c**) uncalcined 0.5% Pt-12% Co/SiO_2 from cobalt acetate.

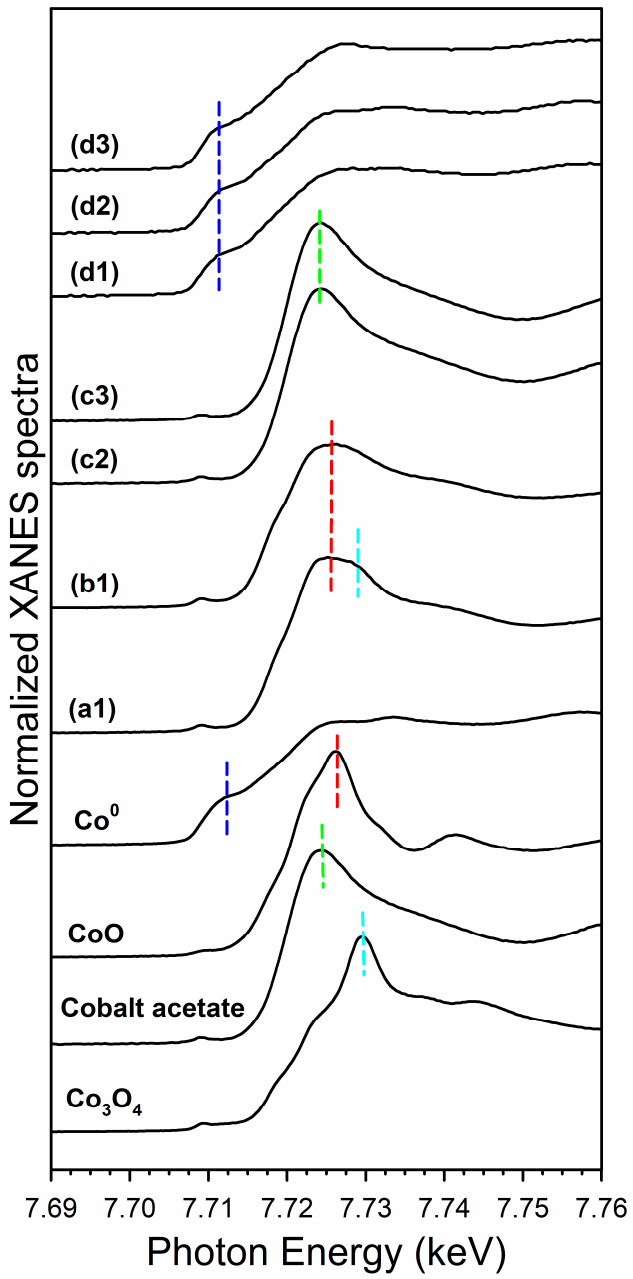

Figure 6. XANES snapshots of references for Co_3O_4, CoO, and Co^0 obtained from the TPR-XANES trajectory of the calcined 25% Co/Al_2O_3 reference catalyst and for cobalt acetate obtained in the initial spectrum of the uncalcined unpromoted catalyst. XANES snapshot spectra for samples prepared from cobalt acetate along the TPR trajectory include (1) the calcined catalyst, (2) the uncalcined catalyst and (3) the uncalcined catalyst with 0.5% Pt promoter at (**a**) the point of maximum spinel (e.g., Co_3O_4), (**b**) the point of maximum CoO following reduction of the spinel, (**c**) the point of maximum cobalt acetate content, and (**d**) the point of maximum Co^0 content following TPR. Dashed lines emphasize the presence of (green) Co^{2+} in cobalt acetate, (cyan) Co^{3+} (i.e., in addition to Co^{2+}) in the spinel, (red) Co^{2+} in CoO, and (blue) Co^0.

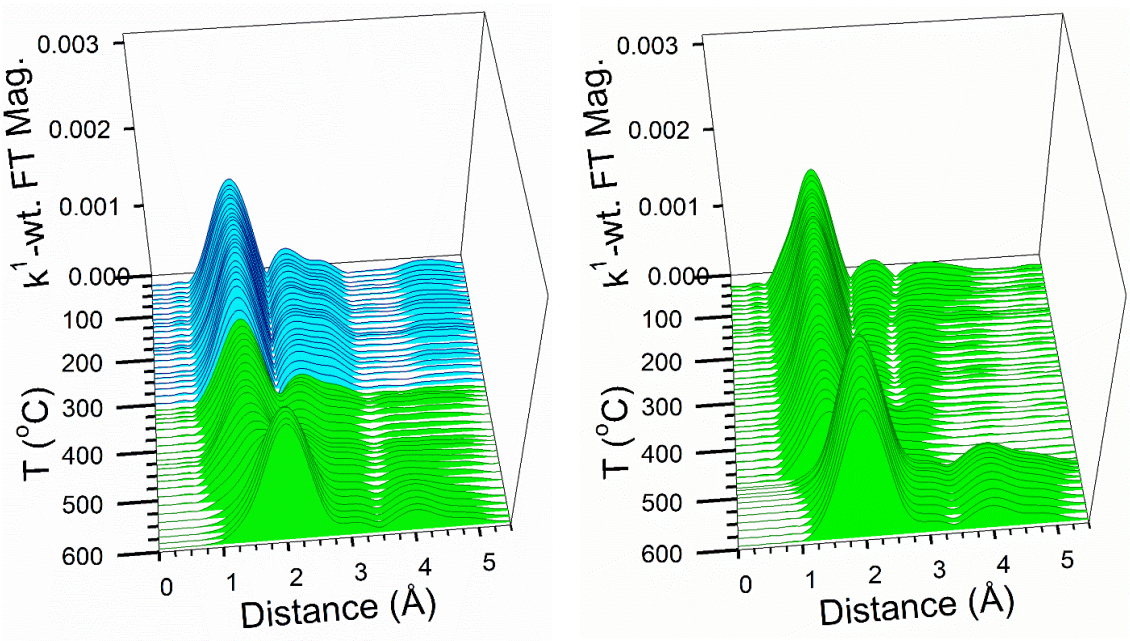

(**a**) (**b**)

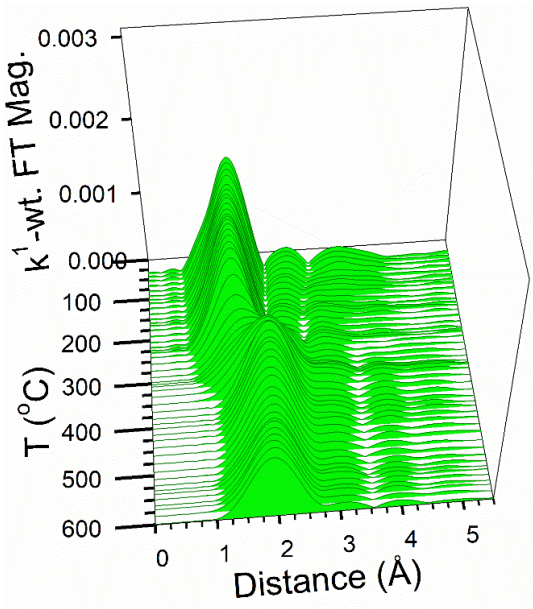

(**c**)

Figure 7. TPR-EXAFS profiles of (**a**) calcined 12% Co/SiO_2 from cobalt acetate, (**b**) uncalcined 12% Co/SiO_2 from cobalt acetate, and (**c**) uncalcined 0.5% Pt-12% Co/SiO_2 from cobalt acetate.

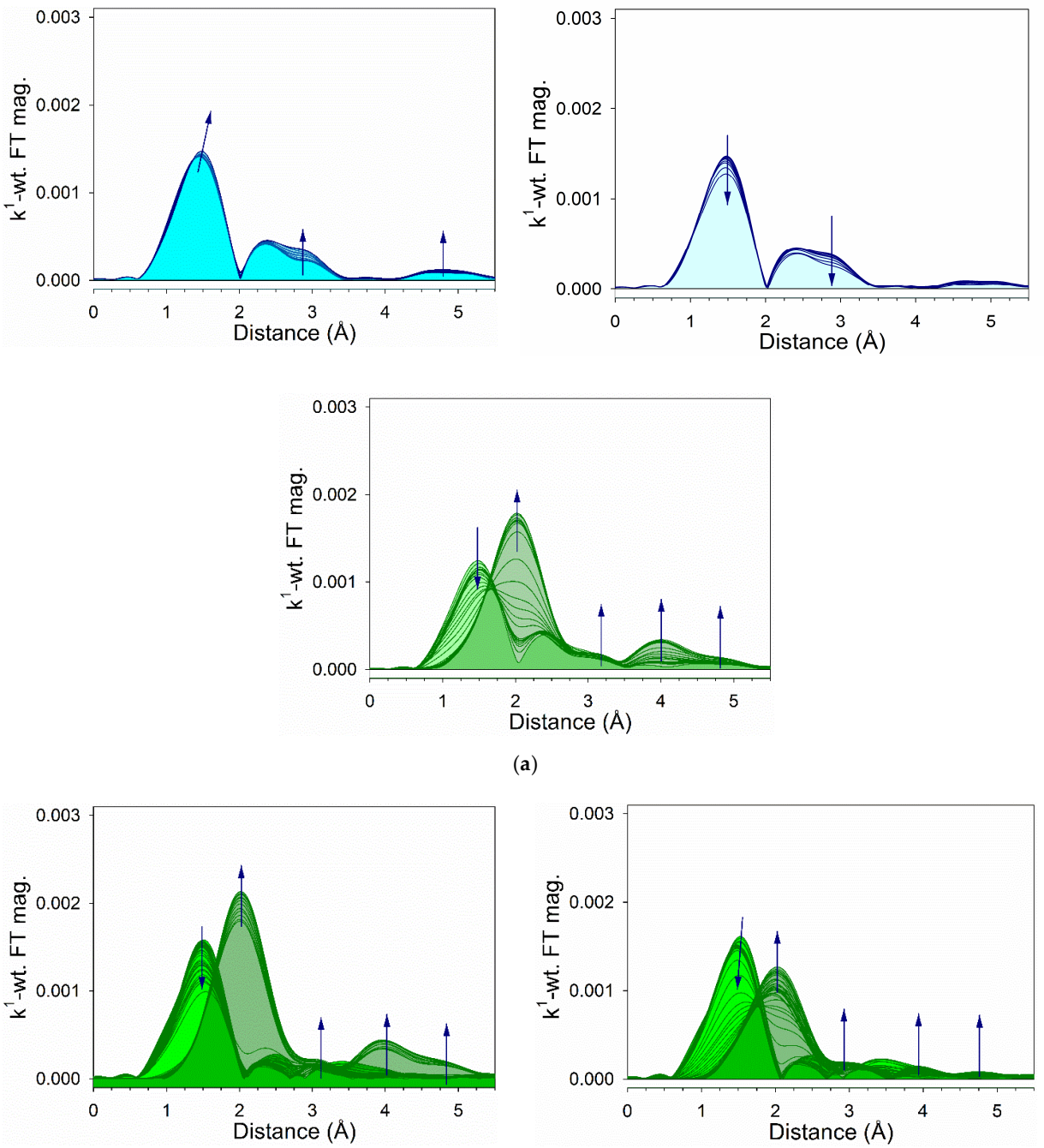

(**a**)

(**b**) (**c**)

Figure 8. TPR-EXAFS profiles for the different temperature regions of (**a**) calcined 12% Co/SiO_2 from cobalt acetate, (**b**) uncalcined 12% Co/SiO_2 from cobalt acetate, and (**c**) uncalcined 0.5% Pt-12% Co/SiO_2 from cobalt acetate.

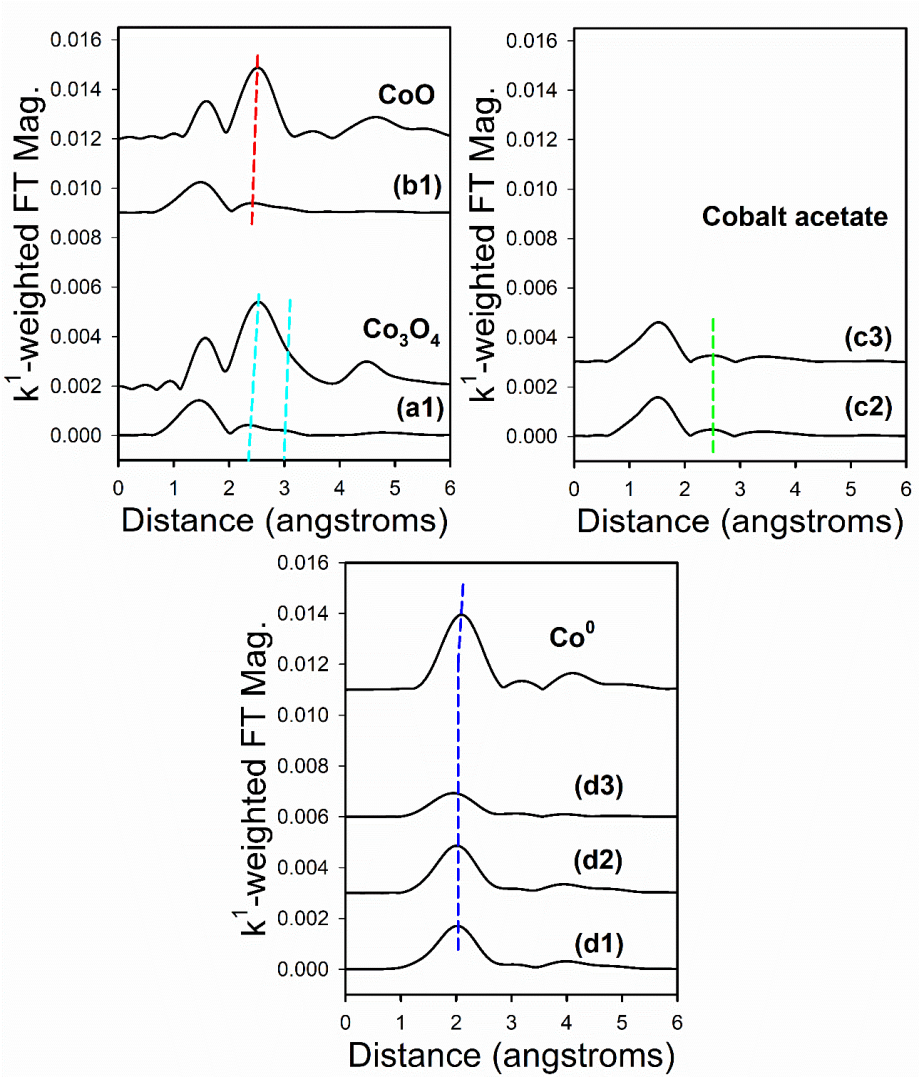

Figure 9. EXAFS snapshots of references for Co_3O_4, CoO, and Co^0 obtained from TPR-XANES trajectory of the calcined 25% Co/Al_2O_3 reference catalyst and for cobalt acetate obtained in the initial spectrum of the uncalcined unpromoted 12% Co/SiO_2 catalyst. EXAFS snapshot spectra for 12% Co/SiO_2 prepared from cobalt acetate along the TPR trajectory include (1) calcined catalyst, (2) uncalcined catalyst and (3) uncalcined catalyst with 0.5% Pt promoter at (**a**) the point of maximum spinel (e.g., Co_3O_4), (**b**) the point of maximum CoO following the reduction of the spinel, (**c**) the point of maximum cobalt acetate content, and (**d**) the point of maximum Co^0 content following TPR. Dashed lines emphasize the presence of Co-Co coordination in (green) cobalt acetate, (cyan) the cobalt spinel, (red) CoO, and (blue) Co^0 nanoparticles.

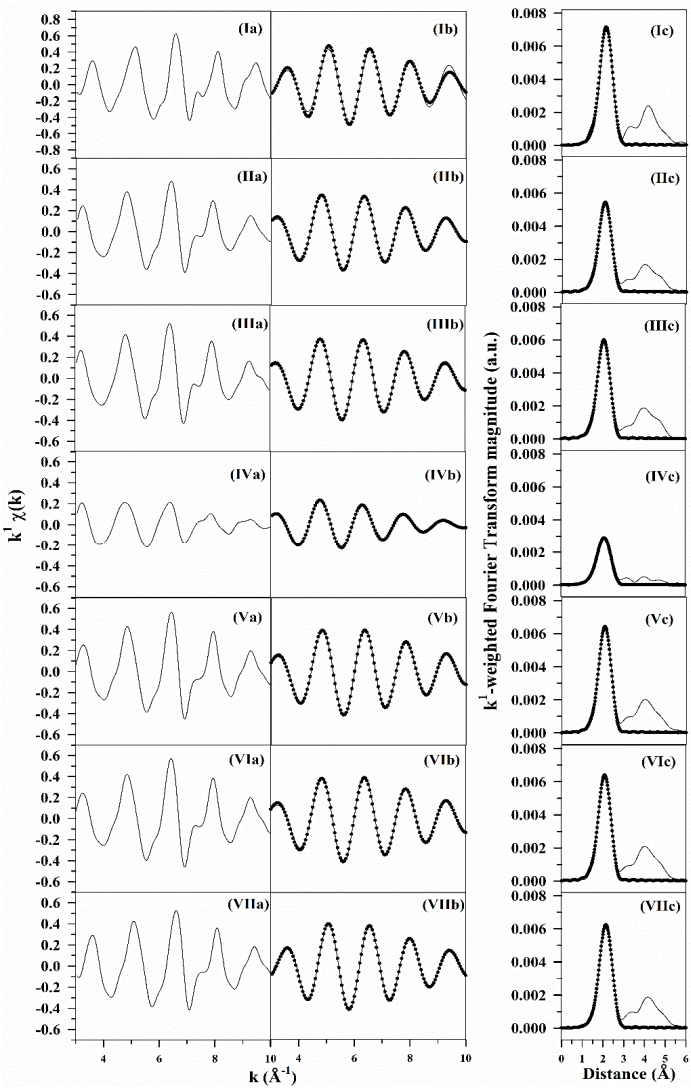

Figure 10. EXAFS fittings after H_2-TPR and cooling, including (**a**) raw k^1-weighted χ(k) data, (**b**) (solid line) filtered k^1-weighted χ(k) data and (filled circles) the results of the fittings, and (**c**) (solid line) raw k^1-weighted Fourier transform magnitude and (filled circles) the results of the fittings for (I) Co^0 foil (note different scale), (II) calcined 12% Co/SiO_2 from cobalt acetate, (III) uncalcined 12% Co/SiO_2 from cobalt acetate, (IV) III with 0.5% Pt, (V) calcined 12% Co/SiO_2 from cobalt chloride, (VI) uncalcined 12% Co/SiO_2 from cobalt chloride, and (VII) VI with 0.5% Pt. The catalysts were treated at up to 600 °C in hydrogen.

Phase-uncorrected TPR-EXAFS spectra are shown in an overhead view in Figure 7a (cyan), a front view in Figure 8a (cyan), and as EXAFS snapshot spectra in Figure 9 (top left, a1,b1). The changes in Co-O and Co-Co coordination are consistent with the conversion of the Co_3O_4 particles to CoO. As shown in Figure 8a, the conversion of Co_3O_4 to CoO includes two parts. As the temperature is first increased to 166 °C (darker cyan), there is a sharpening of the Co-O and Co-Co coordination peaks in Co_3O_4; from 166 to 300 °C, there are decreases (lighter cyan) in the Co-O (~1.5 Å) and Co-Co coordination (~2.9 Å) peaks as Co_3O_4 is converted to CoO. Then, the green spectra reveal decreases in the Co-O (~1.4 Å) and Co-Co (~2.4 Å) coordination peaks for CoO and an increase in the Co-Co metal (~2.0 Å) coordination, in agreement with the TPR-XANES discussion regarding the formation of Co^0. The final spectrum after TPR is Figure 9(d1), where the dashed line shows that Co-Co metal coordination has formed. EXAFS fittings were performed after H_2-TPR and cooling, and the results are depicted in Figure 10. The coordination number after cooling was found to be 9.0 (Table 2), which is near the middle of the range of the catalysts tested (8.6–9.6).

Table 2. EXAFS fittings for Co K-edge data for catalysts following TPR and cooling. Ranges: Δk = 3–10 Å^{-1}; ΔR = 1.0–2.82 Å. S_0^2 was assumed to be 0.90. ** Fixed parameter.

Sample Description	Calcination	N Co-Co Metal	R Co-Co (Å) Metal	e_0 (eV)	σ^2 (Å^2)	r-Factor
Co^0 foil	-	12 **	2.489 (0.010)	6.34 (1.28)	0.00804 (0.00062)	0.019
12% Co/SiO_2 from cobalt acetate	Yes	9.0 (0.42)	2.491 (0.0036)	−3.54 (0.470)	0.00736 (0.00052)	0.0018
12% Co/SiO_2 from cobalt acetate	No	9.3 (0.44)	2.487 (0.0037)	−4.15 (0.486)	0.00674 (0.00052)	0.0018
0.5% Pt-12% Co/SiO_2 from cobalt acetate	No	8.6 (0.82)	2.514 (0.0083)	−3.20 (0.916)	0.0135 (0.00125)	0.0066
12% Co/SiO_2 from cobalt chloride	Yes	9.3 (0.42)	2.488 (0.0035)	−2.41 (0.461)	0.00611 (0.00049)	0.0017
12% Co/SiO_2 from cobalt chloride	No	9.0 (0.41)	2.487 (0.0035)	−2.93 (0.467)	0.00580 (0.00049)	0.0018
0.5% Pt-12% Co/SiO_2 from cobalt chloride	No	9.6 (0.37)	2.489 (0.0029)	6.23 (0.368)	0.00707 (0.00043)	0.0012

The cobalt cluster size from H_2-chemisorption/pulse reoxidation (Table 3) is more relevant to the activated catalyst for use in reaction testing. After reduction at 350 °C for 10 h in hydrogen, the extent of reduction was relatively low (~18.1%) for the unpromoted calcined catalyst; however, adding 0.5% Pt significantly improved the reduction of the smaller cobalt oxide species in interaction with the support. Not only did the extent of reduction increase from 18.1 to 35.9%, but the average Co cluster diameter decreased from 12.0 to 7.8 nm. As we have noted in previous investigations, decreasing the cluster size typically has a more pronounced impact on the Co site density than improved reducibility; nevertheless, both factors contribute to a boost in the active site density, where the micromoles of H_2 desorbed per gram of catalyst increased from 16.3 to 49.5 by adding 0.5% Pt. The latter value is among the highest reported for cobalt silica catalysts. The active site density is a factor 4.6 times higher than that of a H_2-activated conventional air-calcined catalyst (10.8 micromoles of H_2 desorbed per gram of catalyst) [32] and 26% higher than our prior best catalyst prepared from the direct H_2 reduction of cobalt nitrate and containing Pt promoter (39.2 micromoles of H_2 desorbed per gram of catalyst). The trend in cobalt diameter matched that of the cobalt domain size from XRD using the integral breadth method (Tables 3 and 4).

Table 3. Results of hydrogen chemisorption, pulse reoxidation, and X-ray diffraction. ** Positive peak in the TCD signal indicates the desorption of a Cl compound (e.g., HCl).

Catalyst	Calcined?	H_2 Desorbed per g cat (μmol/g_{cat})	Uncorr. % Disp.	Uncorr. Average Cluster Diam. (nm)	% Red.	Corr. % Disp.	Corr. AverageCluster Diam. (nm)	Average Est'd Domain Diam. from XRD
12% Co/SiO_2 from cobalt acetate	Yes	16.3	1.56	66.4	18.1	8.6	12.0	17.8
12% Co/SiO_2 from cobalt acetate	No	4.4	0.57	180.9	9.1	6.3	16.6	21.6
0.5% Pt-12% Co/SiO_2 from cobalt acetate	Yes	49.5	4.74	21.9	35.9	13.2	7.8	7.2
0.5% Pt-12% Co/SiO_2 from cobalt acetate	No	21.4	2.80	37.1	52.1	5.5	19.5	19.2
12% Co/SiO_2 from cobalt chloride	Yes	**	-	-	18.6	-	-	31.7
12% Co/SiO_2 from cobalt chloride	No	**	-	-	56.0	-	-	33.1
0.5% Pt-12% Co/SiO_2 from cobalt chloride	Yes	3.3	0.31	334	54.6	0.6	182.2	24.0
0.5% Pt-12% Co/SiO_2 from cobalt chloride	No	6.2	0.79	153	57.7	1.3	85.8	30.2

Table 4. Results of X-ray diffraction from the integral breadth method.

Catalyst	Calcined?	Co^0 HCP (100) Position (2θ in °)	Co^0 (100) Average Crystallite Domain Diameter (nm)	* Co^0 HCP (002) Position (2θ in °)	Co^0 (002) Average Crystallite Domain Diameter (nm)	Co^0 HCP (101) Position (2θ in °)	Co^0 (101) Average Crystallite Domain Diameter (nm)	Average Crystallite Diameter from the 3 Peaks (nm)
12% Co/SiO_2 from Cobalt Acetate	Yes	-	-	44.71	17.8	-	-	-
0.5% Pt-12% Co/SiO_2 from Cobalt Acetate	Yes	-	-	44.65	7.2	-	-	-
12% Co/SiO_2 from Cobalt Acetate	No	41.62	18.7	44.32	19.4	47.31	26.8	21.6
0.5% Pt-12% Co/SiO_2 Cobalt Acetate	No	41.58	22.1	44.47	14.7	47.43	20.8	19.2
12% Co/SiO_2 from Cobalt Chloride	Yes	41.62	33.0	44.48	29.5	47.51	32.7	31.7
0.5% Pt-12% Co/SiO_2 from Cobalt Chloride	Yes	41.54	31.9	44.52	19.9	47.41	20.3	24.0
12% Co/SiO_2 from Cobalt Chloride	No	41.50	45.6	44.49	21.4	47.38	32.3	33.1
0.5% Pt-12% Co/SiO_2 from Cobalt Chloride	No	41.76	26.8	44.47	28.3	47.43	35.6	30.2

* Peaks may contain a contribution from FCC cobalt, including (111) at ~44.2° and (220) at ~75.9°. No peak detected at 51.5° for (200) to show the formation of FCC Co^0. Additional HCP Co^0 peaks observed at 62.7° for (102) and 84.2° for (103).

Mohamed et al. [43] investigated the decomposition of cobalt acetate tetrahydrate using TG, differential thermal gravimetry (DTG), differential thermal analysis (DTA) and DSC techniques in different atmospheres, including N_2, H_2, and air. Major ranges included 30–140 °C, where cobalt acetate lost three waters of hydration; 223–251 °C, where $Co(CH_3COO)_2 \cdot H_2O$ was converted to $(CH_3COO)_2Co(COCH_3)$ by reaction with acetic anhydride, resulting in the formation of acetic acid; 250–290 °C, where the reaction of the preceding complex with liberated H_2O produced $(CH_3COO)_2$Co-OH and acetaldehyde; and 315–360 °C, where the compound decomposed to produce CoO, with a reduction in the presence of hydrogen to Co^0 liberating acetic acid and H_2O.

Figure 3b (black) shows that the direct H_2 reduction of cobalt acetate supported on silica tended to broaden the TPR profile to higher temperatures (e.g., up to 900 °C), and the H_2 uptake peaks in TPR-MS (Figure 4c) are consistent with this. The H_2O evolution in TPR-MS (Figure 4c) is consistent with losses in waters of hydration, as well as reduction events. To gain insight into the temperature at which cobalt acetate decomposed, MS signals for acetaldehyde, CO_2, CH_4, and CO were followed (Figure 4c). Cobalt acetate began to decompose above 300 °C, where acetaldehyde and CO_2 were major peaks, with CH_4 being a minor product. Interestingly, the TPR (Figure 3b, red) and TPR-MS profiles (Figure 4d) show that adding 0.5% Pt resulted in facile reduction below 350 °C, with no high-temperature peaks being detected. However, the cobalt acetate decomposition peaks were different in nature, suggesting a different decomposition pathway. While acetaldehyde and CO_2 dominated the profiles of the unpromoted catalyst, CH_4 and CO were the main decomposition products of cobalt acetate decomposition for the 0.5% Pt-promoted uncalcined catalyst. The TPR-EXAFS/XANES spectra of these catalysts (green only) revealed the conversion of cobalt acetate to cobalt metal (Figure 5b,c for unpromoted and Pt-promoted, respectively). In the XANES snapshot spectra shown in Figure 6 (c2 and c3 for unpromoted and Pt-promoted, respectively), the catalysts begin with the line shape of Co^{2+} consistent with cobalt acetate species. These species are directly converted to Co^0, as shown in Figure 5b,c) and Figure 6 (spectra d2 and d3). One important aspect to note is that spectrum d3 in Figure 6 of the Pt-promoted catalyst still retains a low-intensity white line (~7.727 keV), suggesting that the more severe decomposition of cobalt acetate via decarbonylation resulted in the formation of a fraction of cobalt carbide (e.g., compared with the cobalt carbide spectrum from [44]).

The phase-uncorrected TPR-EXAFS spectra in Figure 7b,c and Figure 8b,c show losses in Co-O coordination (~1.5 Å) in cobalt acetate and increases in Co-Co metal (~2.0 Å) coordination. The EXAFS snapshots in Figure 9 before (c2 and c3) and after TPR (d2 and d3) emphasize these changes. In EXAFS fittings following TPR and cooling to ambient conditions, the Pt-promoted Co/SiO_2 catalyst derived from the direct reduction of cobalt acetate displayed differences from the other catalysts. The envelope function (Figure 10, spectrum IVa) had smaller amplitude, resulting in a smaller Fourier transform magnitude peak (Figure 10, spectrum IVc). The fitting of the spectrum resulted in the smaller Co-Co coordination number for Co^0 of 8.6 (Table 2). Moreover, the Co-Co metallic distance was slightly longer than that of the Co metal foil (2.514 Å relative to 2.489 Å), suggesting the inclusion of carbon within the structure and consistent with the small white line for cobalt carbide observed in the XANES profile. Moreover, Table 2 shows that the level of disorder as measured by the Debye-Waller factor was approximately double for this catalyst, a result that is also consistent with carbide formation.

In chemisorption/pulse reoxidation measurements (Table 3), the Co^0 surface active site densities of the catalysts prepared by the direct H_2 reduction of cobalt acetate were lower than those of the calcined Pt-promoted Co/silica catalyst, but for different reasons. With the unpromoted catalyst, the extent of reduction was low (9.1%) and only the largest Co species were able to be reduced, resulting in an average Co size of 16.6 nm. For the Pt-promoted uncalcined catalyst, facile reduction as shown in TPR (Figure 3) was confirmed by pulse reoxidation measurements, which showed a % of cobalt reduction of 52.1%. However, the "apparent" cluster size was larger than the optimal catalyst. This may be caused by

facile reduction and the agglomeration of the Co crystallite domains and/or the presence of C on the Co surface, which decreases the Co^0 site density (thus showing up as a larger cluster size in chemisorption). Larger than ideal Co^0 crystallites were confirmed by XRD using the integral breadth method (Tables 3 and 4) for the catalysts derived from the direct H_2 reduction of cobalt acetate (21.6 and 19.2 nm for direct H_2 reduction versus 17.8 and 7.2 nm for air calcination/the H_2 reduction of unpromoted and Pt-promoted catalysts, respectively, prepared from cobalt acetate). Note that XRD measures average domain size, whereas H_2-chemisorption/pulse reoxidation measure cluster size. XRD can overestimate the Co particle size if a fraction of the Co clusters exhibit domains with an insufficient long-range order, while it can underestimate Co particle size if the particles consist of domains of cobalt fused together. Therefore, while the two numbers typically trend in a similar direction, they do not measure the same property.

While the catalysts prepared from cobalt acetate displayed wide differences in structure and reduction behavior through calcination and/or Pt promoter addition, the same was not true of the catalysts prepared using cobalt chloride. After calcination at 350 °C for 4 h, there was very little color change observed for the catalyst (i.e., they remained pink), whereas the cobalt acetate catalysts turned black in color after air calcination. In the TPR and TPR-MS profiles of Figures 3 and 11, it can be seen that there are only small differences in the reduction profiles of the catalysts with (Figures 3c and 11a,b) or without (Figures 3d and 11c,d) calcination and with (Figure 3c,d (red) and Figure 4b,d) or without (Figure 3c,d (black) and Figure 4a,c) 0.5% Pt promoter. All catalysts reduced in the range of 350–500 °C, with only the TPR of the unpromoted calcined catalyst (Figure 3c, black) being shifted to a slightly higher temperature (Δ50 °C from 414 to 464 °C) compared to the other three catalysts.

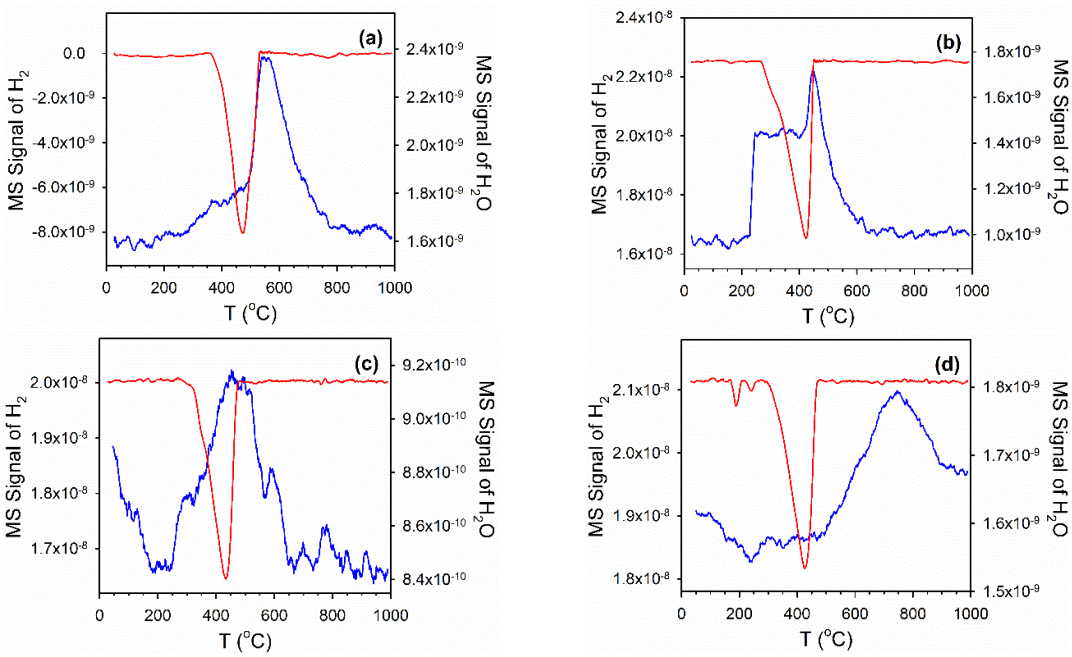

Figure 11. H_2-TPR profiles with the mass spectra analysis of the exhaust gas for 12% Co/SiO_2 catalysts prepared with cobalt chloride, including (**a**) calcined, (**b**) calcined promoted with 0.5% Pt, (**c**) uncalcined, and (**d**) uncalcined promoted with 0.5% Pt. (Red) H_2, (Blue) H_2O.

The TPR-EXAFS/XANES results in Figures 12–16 gave insight into the electronic and structural changes occurring with the catalysts prepared from cobalt chloride and reveal three main events. The first event (shown in red in Figure 12, Figure 14, and Figure 15) takes place between room temperature and 110 °C and is associated with the loss of H_2O from the cobalt chloride salt. While there is little change in the TPR-XANES spectra in this region (moving from a1–3 to b1–3 in Figure 13) for the three catalysts examined, the

TPR-EXAFS spectra in Figures 14 and 15 (a–c, red spectra), and 16 (moving from a1–3 to b1–3) display changes. The asymmetric peak for Co-Cl becomes sharpened, where the shoulder at 1.4 Å decreases and the peak situated at approximately 1.9 Å in the phase-uncorrected FT magnitude spectra slightly increases. The second event involves losses in Co-Cl coordination (pink spectra in Figures 12, 14 and 15, which is highlighted in the EXAFS snapshot spectra (moving from b1–3 to c1–3 in Figure 16). In TPR-XANES (Figure 12, pink spectra), the high-energy shoulder at 7.725 keV is diminished moreso than the low-energy peak containing the maximum. This is emphasized in moving from b1–3 to c1–3 in the TPR-XANES snapshots provided in Figure 13. This event is complete by 338 °C for the calcined catalyst, 305 °C for the uncalcined unpromoted catalyst, and 255 °C for the 0.5% Pt-promoted uncalcined catalyst. The final event, highlighted by the purple TPR-EXAFS spectra in Figures 14 and 15, is a continued decrease in Co-Cl coordination (~1.75 Å) with a concomitant increase in Co-Co coordination in Co^0 (~2 Å). In Figure 16, before and after snapshots for this event are shown in moving from c1–3 to d1–3. In the TPR-XANES spectra (also highlighted in purple) shown in Figure 12, the XANES white line intensity diminishes as metallic cobalt is formed. This final event is completed by ~500 °C for the unpromoted catalysts and by 400 °C for the Pt-promoted one (Figure 12).

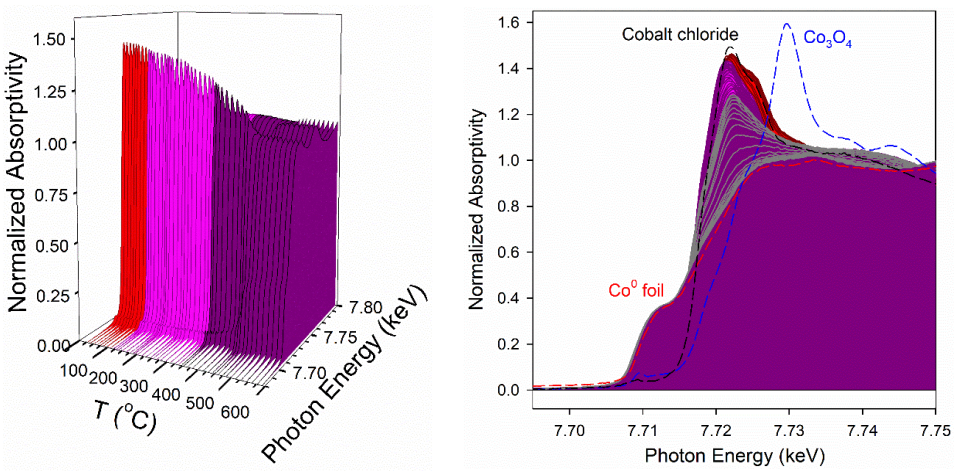

(**a**)

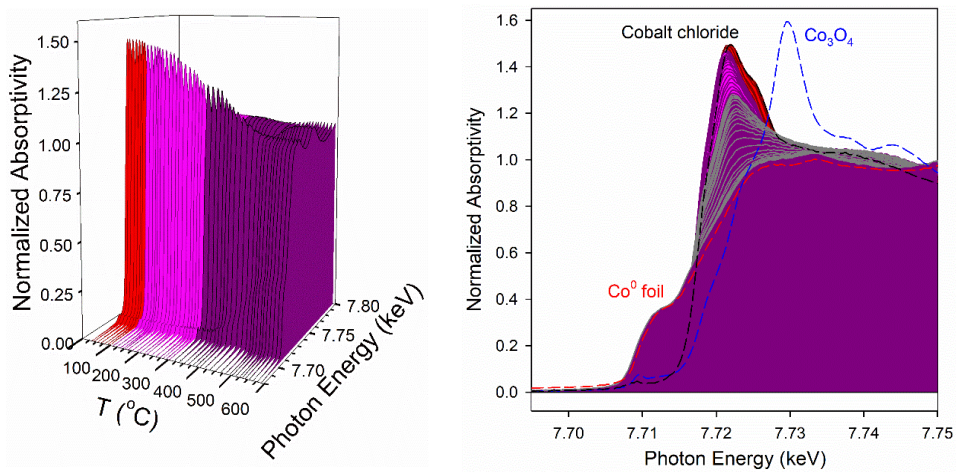

(**b**)

Figure 12. *Cont.*

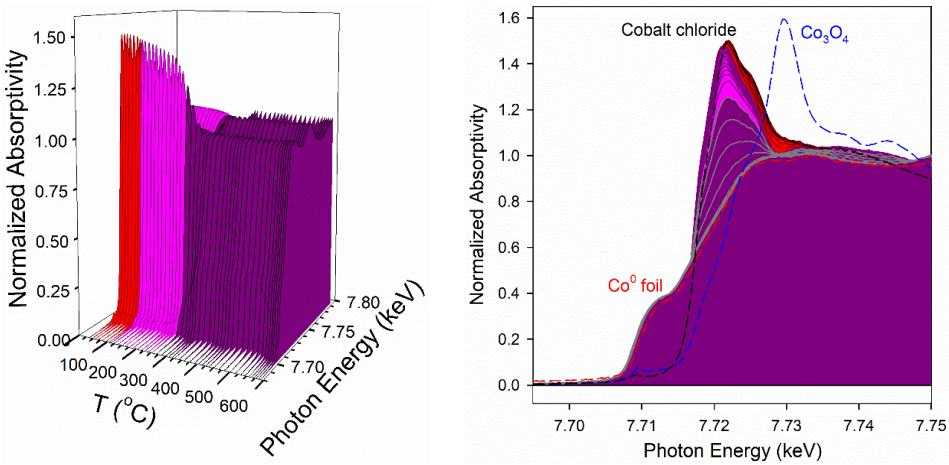

(**c**)

Figure 12. TPR-XANES profiles of (**a**) calcined 12% Co/SiO_2 from cobalt chloride, (**b**) uncalcined 12% Co/SiO_2 from cobalt chloride, and (**c**) uncalcined 0.5% Pt-12% Co/SiO_2 from cobalt chloride.

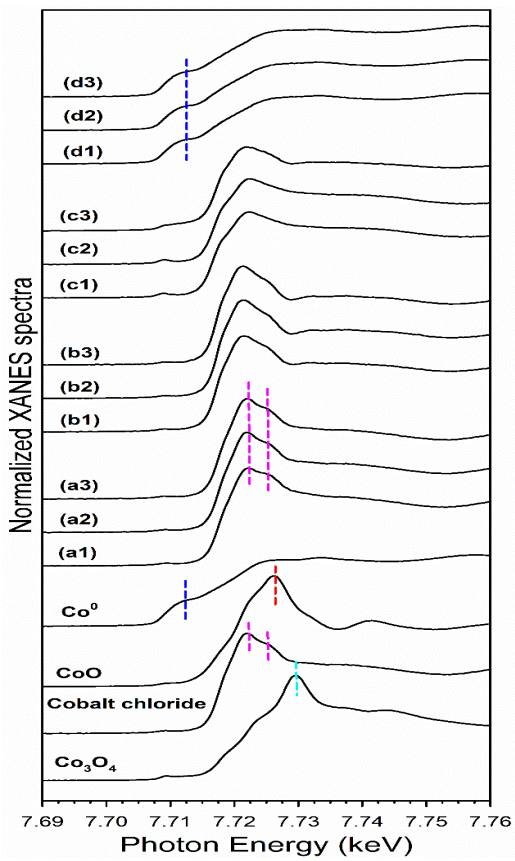

Figure 13. XANES snapshots of (bottom) references for Co_3O_4, CoO, and Co^0 obtained from the TPR-XANES trajectory of the calcined 25% Co/Al_2O_3 catalyst and for the cobalt chloride obtained in the initial spectrum of the uncalcined unpromoted catalyst. XANES snapshot spectra for samples prepared from cobalt chloride along the TPR trajectory include (1) the calcined catalyst, (2) the uncalcined catalyst and (3) the uncalcined catalyst with 0.5% Pt promoter at (**a**) the point of maximum cobalt chloride, (**b**) the point of partial cobalt chloride decomposition #1, (**c**) the point of partial cobalt chloride decomposition #2, and (**d**) the point of maximum Co^0 content following TPR. Dashed lines emphasize: (pink) Co^{2+} in cobalt chloride, (cyan) Co^{3+} (i.e., in addition to Co^{2+}) in the spinel, (red) Co^{2+} in CoO, and (blue) Co^0.

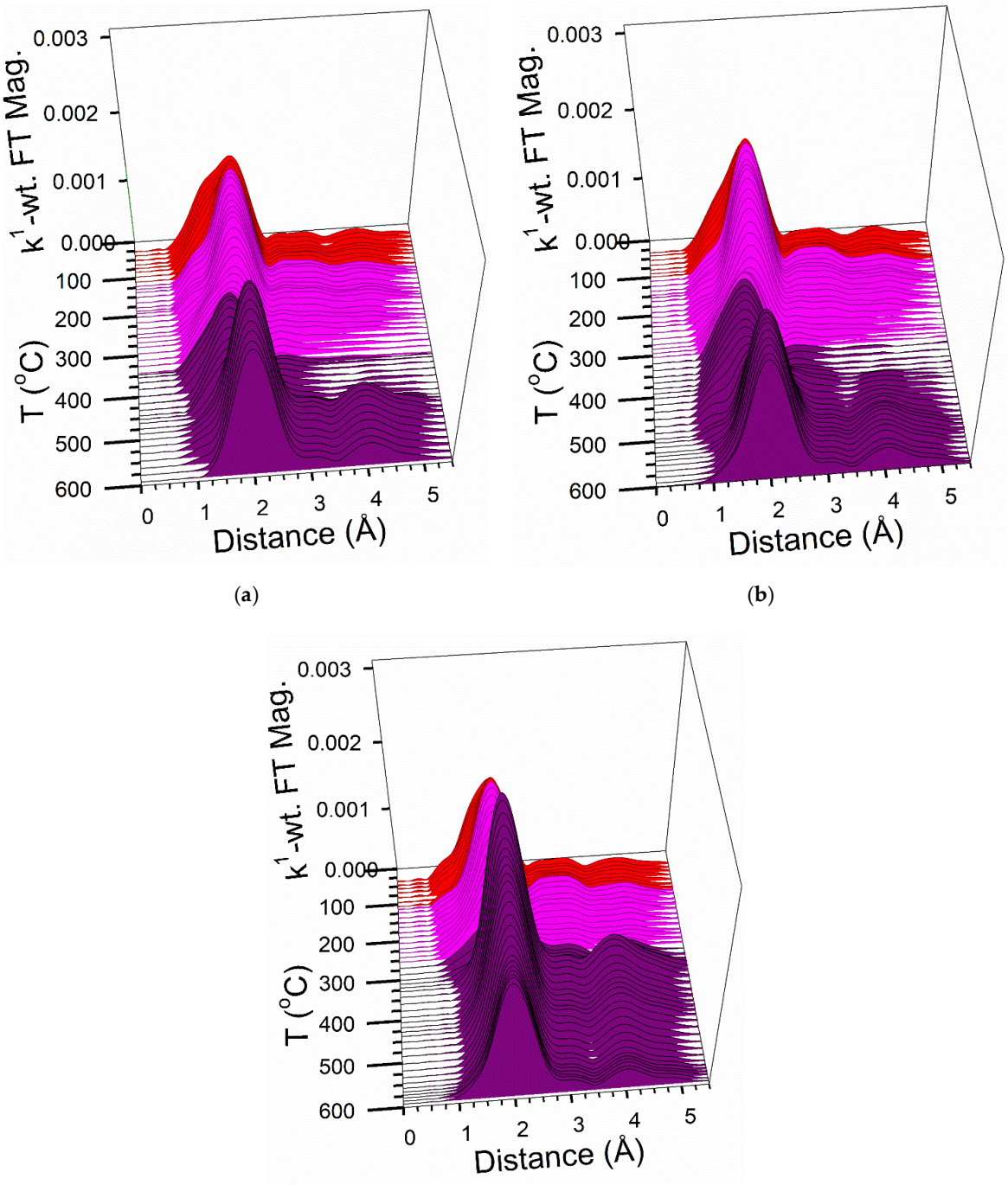

Figure 14. TPR-EXAFS profiles of (**a**) calcined 12% Co/SiO_2 from cobalt chloride, (**b**) uncalcined 12% Co/SiO_2 from cobalt chloride, and (**c**) uncalcined 0.5% Pt-12% Co/SiO_2 from cobalt chloride.

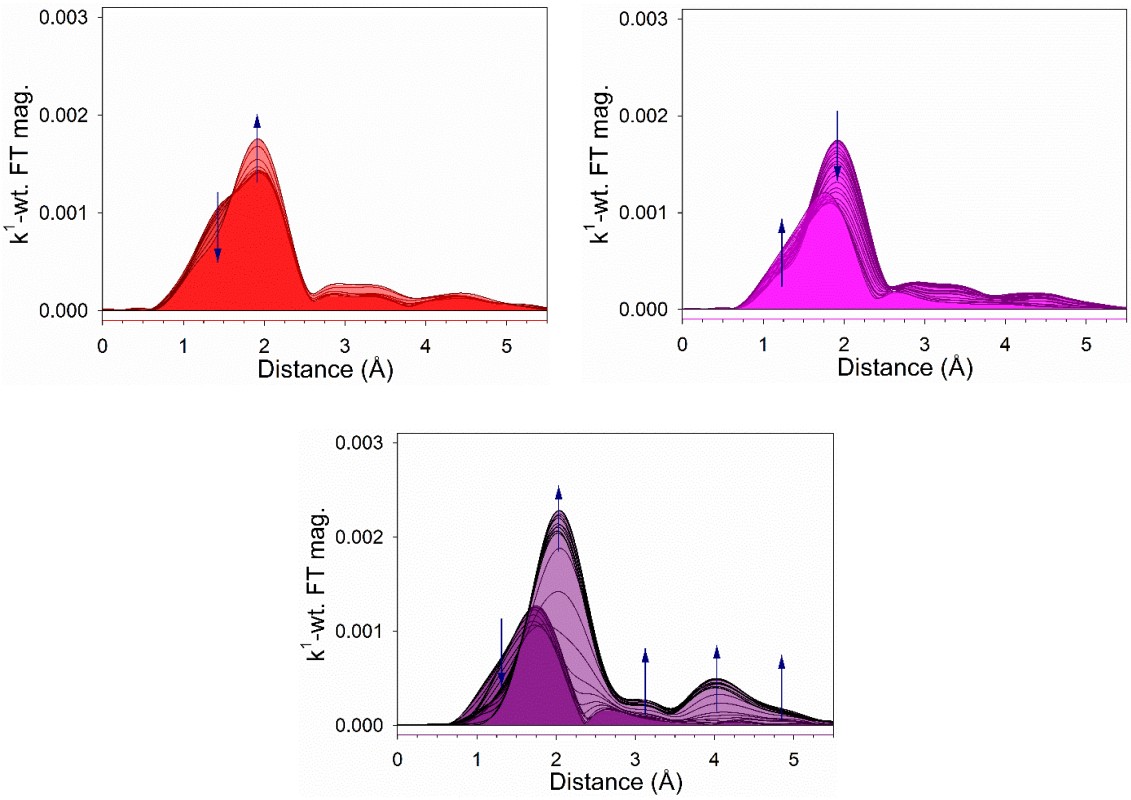

(**a**)

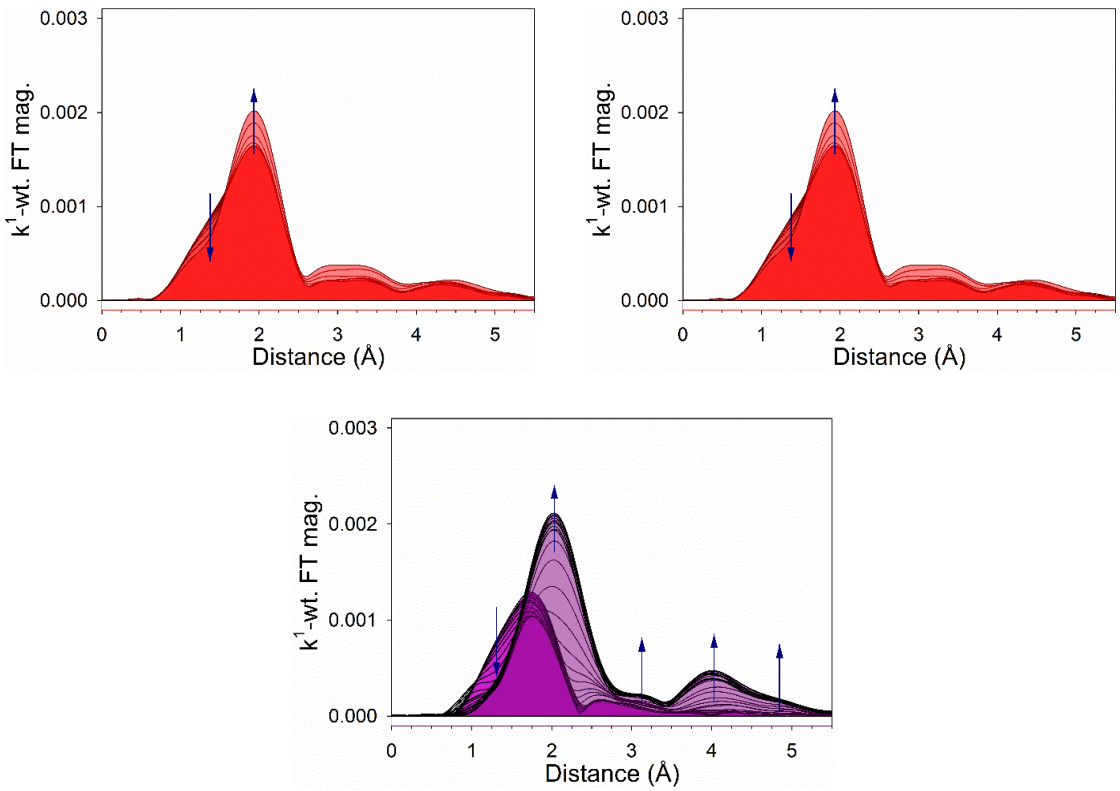

(**b**)

Figure 15. *Cont.*

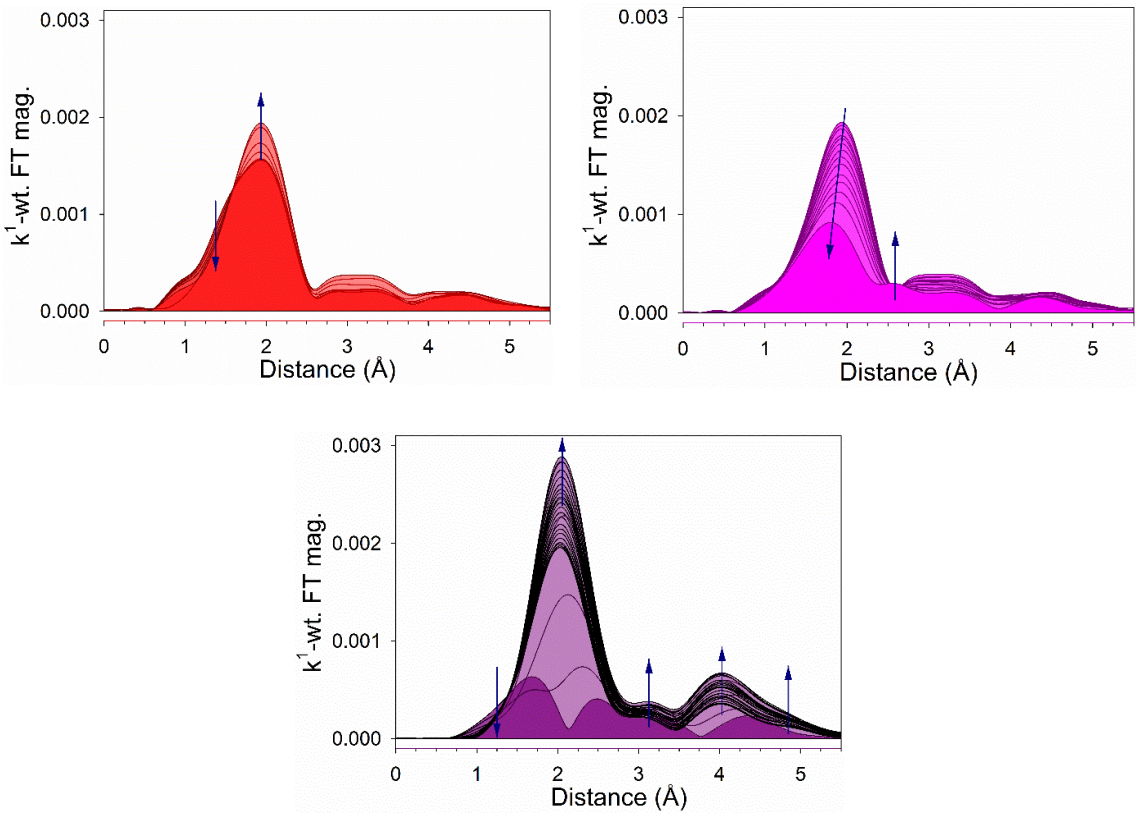

(**c**)

Figure 15. TPR-EXAFS profiles for the different temperature regions of (**a**) calcined 12% Co/SiO_2 from cobalt chloride, (**b**) uncalcined 12% Co/SiO_2 from cobalt chloride, and (**c**) uncalcined 0.5% Pt-12% Co/SiO_2 from cobalt chloride.

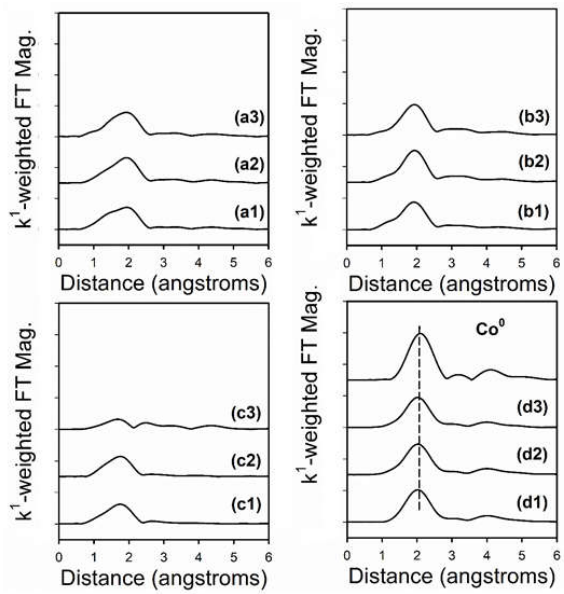

Figure 16. EXAFS snapshots of (**bottom right**) reference Co^0 obtained from TPR-XANES trajectory of the calcined 25% Co/Al_2O_3 catalyst. EXAFS snapshot spectra for samples prepared from cobalt chloride along the TPR trajectory, including (1) the calcined catalyst, (2) the uncalcined catalyst, and (3) the uncalcined catalyst with 0.5% Pt promoter at (**a**) the point of maximum cobalt chloride, (**b**) the point of partial cobalt chloride decomposition #1, (**c**) the point of partial cobalt chloride decomposition #2, and (**d**) the point of maximum Co^0 content following TPR. Dashed line: 1st shell Co-Co coordination in Co^0.

Figure 10 reveals the EXAFS Fourier transform magnitude spectra of these catalysts (Vc–VIIc), where the peaks for Co-Co coordination tend to be larger than those of the corresponding catalysts derived from cobalt acetate (IIc–IVc). The EXAFS fittings in Table 2 revealed very high coordination numbers (9.0–9.6) for these catalysts after TPR and cooling. In chemisorption with pulse reoxidation (Table 3), the catalysts prepared from cobalt chloride that we were able to measure had the lowest cobalt active site densities (up to 6.2 micromoles of H_2 desorbed per gram of catalyst). For the unpromoted catalysts, a positive peak during temperature-programmed desorption suggests that after reduction at normal activation temperature (350 °C in hydrogen), residual chlorine remains on the cobalt surface. H_2 TPR for the cobalt chloride catalysts involves the formation and removal of HCl, and the positive peak relative to Ar as the reference gas is consistent with HCl desorption (note: H_2 evolution relative to Ar gives a negative peak).

3.3. Catalytic Activity

Referring to the results and data provided in the previous section, not all of the catalysts are suitable for use in an FTS reactor. The results show that applying cobalt chloride as a precursor results in very large cobalt clusters (e.g., 86 and 182 nm) and a very low cobalt active site density due to weak interactions between Co species and the support, resulting in large Co particles; moreover, residual chlorine also caused the site blocking of cobalt. The Pt-Co/silica catalysts prepared from cobalt chloride exhibited an extremely poor activity (Figure 17), with CO conversions of less than 4%.

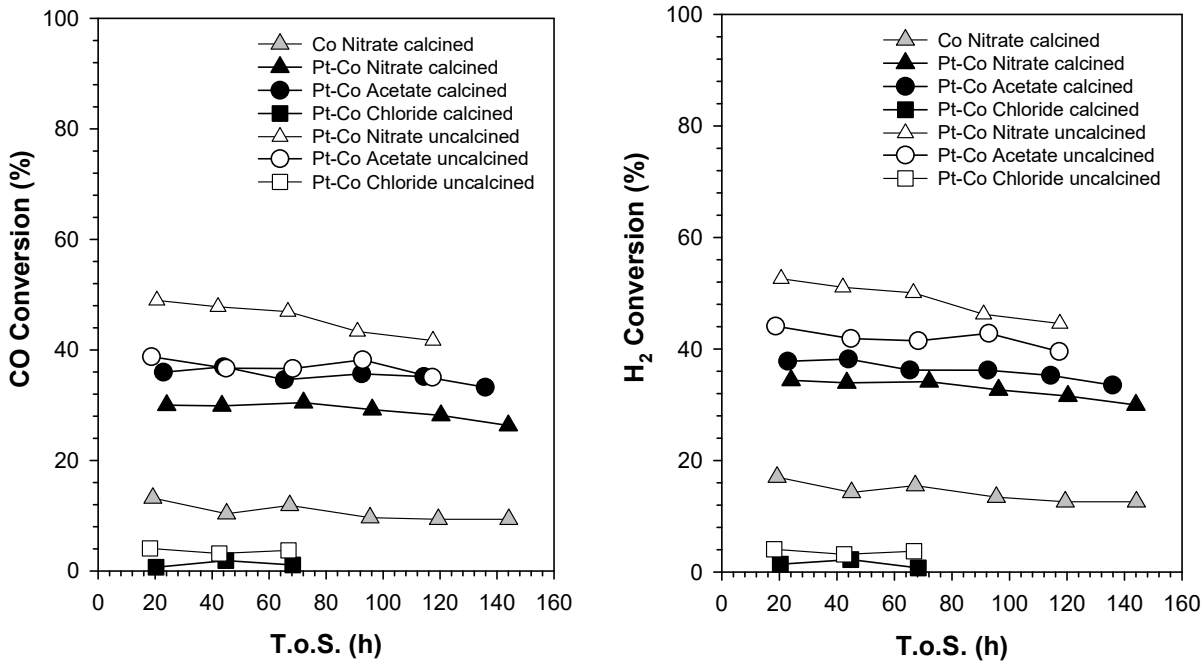

Figure 17. (**left**) CO conversion and (**right**) H_2 conversion from catalytic testing in the CSTR (T = 220 °C, P = 20 atm, H_2/CO = 2 mol/mol, SV = 6 slph/g_{cat}).

Although the extent of the reduction of H_2-reduced uncalcined Pt-Co/silica catalyst was high (52%), the cobalt particle diameter of 19.5 nm was somewhat larger than the ideal size (e.g., 8–15 nm) and resulted in a relatively low cobalt active site density. The catalyst that was significantly better in terms of the cobalt active site density from chemisorption was the Pt-Co/silica catalyst prepared using the air calcination of cobalt acetate prior to H_2 activation.

Figure 17 compares the CO and H_2 conversion rates versus time on-stream (T.O.S) for the H_2-activated air-calcined Pt-Co/SiO_2 catalyst prepared from cobalt acetate versus the H_2-activated Pt-Co/SiO_2 catalyst from the conventional air calcination of cobalt nitrate.

Both conversions trended in a similar manner. The CO conversion rate of conventional (using cobalt nitrate as precursor) calcined, 0.5% Pt-12% Co/SiO_2, started around 30% then the catalyst activity decreased to 27% after 190 h. The CO conversion rate of the novel catalyst (using cobalt acetate as precursor), 0.5% Pt-12% Co/SiO_2, started at 38% and decreased to 33% after the same period of time. The catalyst prepared by the direct reduction of cobalt acetate was similar to that of the counterpart air-calcined/H_2-reduced catalyst. This is a 20–25% improvement in relative activity on a per gram catalyst basis. Based on the chemisorption results, the air-calcined/H_2-reduced Pt-Co/silica catalyst prepared from cobalt acetate was expected to have higher CO conversion than that of the Pt-Co/silica prepared from direct cobalt nitrate reduction, our best cobalt/silica catalyst to date in terms of activity (49.5 μmol/g_{cat} versus 39.2 μmol/g_{cat}). Instead, it had 75% of the activity of the latter catalyst. This is not surprising, considering that the Pt-Co/silica catalyst prepared from cobalt acetate (calcination/reduction) had very strong interactions with the support (TPR). The results suggest that a fraction of tiny cobalt nanoparticles formed from these species during activation and were likely reoxidized by indigenous H_2O from the FTS reaction, as it is known that Co^0 particles below 2–4 nm are unstable. Another possibility is that residual carbon in the catalyst, present as cobalt carbide, hindered the activity. Both the Pt-Co/silica catalysts prepared from cobalt acetate exhibited good stability and an approximately three times higher CO conversion than unpromoted Co/silica prepared using the traditional methods of cobalt nitrate, air calcination, and H_2 reduction.

Figure 18 reveals that the selectivity of the Pt-promoted Co/silica catalysts prepared from cobalt acetate performed significantly worse than the corresponding catalysts prepared from cobalt nitrate. The methane selectivity, C_2–C_4 selectivity, and C_{5+} selectivities were 15–18%, 20–30%, and 60–70% for the Pt-Co/silica catalysts derived from cobalt acetate, while they were 8–10%, 10–12%, and 80% for the Pt-Co/silica catalysts derived from cobalt nitrate. As selectivity is a function of conversion, a better comparison of selectivity was made by comparing selectivity at similar conversion levels with various space velocities. Table 5 shows that for CO conversions in the range of 45.1–48.2%, the C_1–C_4 selectivity was higher for the Pt-Co/SiO_2 catalysts derived from cobalt acetate (32.2% air-calcined and 38.7% uncalcined) relative to the catalysts derived from cobalt nitrate (17.5–18.6%). Moreover, the chain growth probability (α) values were lower for the Pt-Co/SiO_2 catalysts derived from cobalt acetate (0.766 air-calcined and 0.693 uncalcined) relative to the catalysts derived from cobalt nitrate (0.789–0.792). Finally, as shown in Figure 19, the olefin fractions (light blue bars) tended to be lower and paraffin fractions (dark blue bars) correspondingly higher for the Pt-Co/SiO_2 catalysts derived from cobalt acetate relative to the catalysts derived from cobalt nitrate. Higher light gas selectivities, lower α-values, and lower olefin fractions are typical of catalysts exhibiting excessive hydrogenation.

Table 5. CO conversion and product selectivity for the catalysts tested at similar CO conversions (process conditions: T = 220 °C, P = 300 psi, H_2/CO = 2 mol/mol, SV varied).

Catalyst	CO Conversion [%]	Selectivity [%]				α for C_{10}-C_{17}
		CH_4	C_2-C_4	C_{5+}	CO_2	
Co/SiO_2 Nitrate calcined	48.2	8.3	9.2	81.4	1.1	-
Pt-Co/SiO_2 Nitrate uncalcined	48.9	8.0	10.2	81.5	0.3	0.792
Pt-Co/SiO_2 Nitrate calcined	45.4	8.5	10.1	80.5	0.9	0.789
Pt-Co/SiO_2 Acetate uncalcined	45.1	13.5	25.2	58.7	2.5	0.693
Pt-Co/SiO_2 Acetate calcined	47.1	12.6	19.6	65.9	1.9	0.766

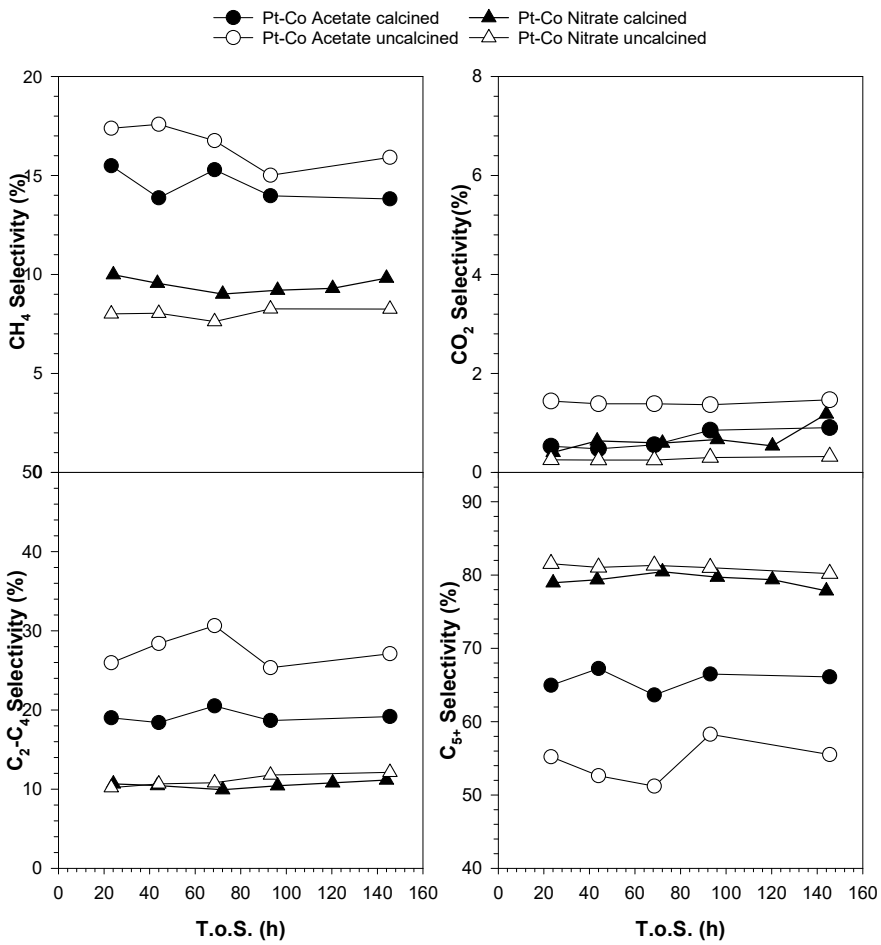

Figure 18. Selectivity results of catalyst testing in the CSTR (T = 220 °C, P = 20 atm, H_2/CO = 2 mol/mol, SV = 6 slph/g_{cat}).

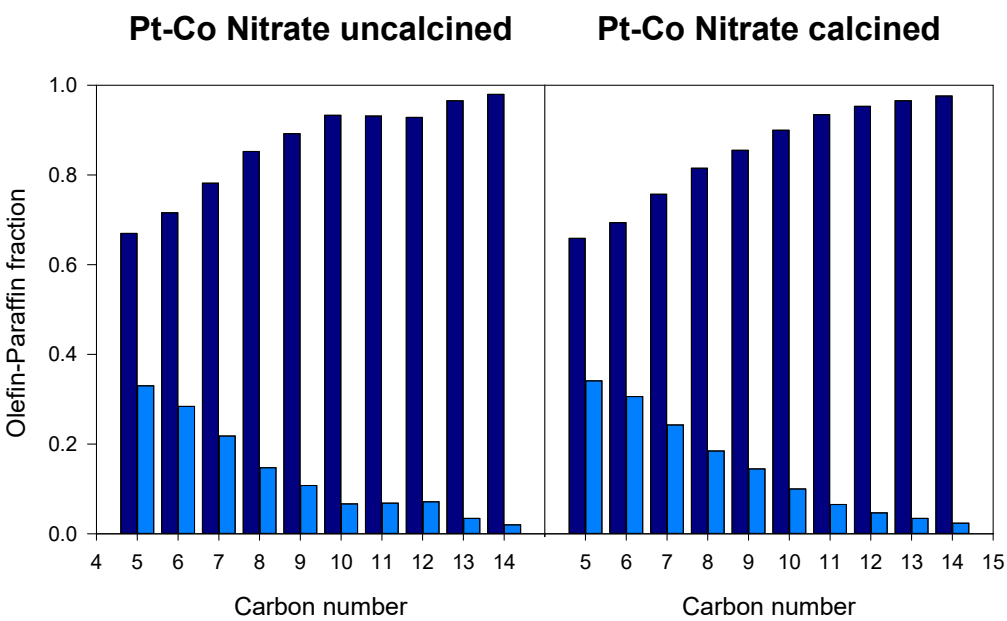

Figure 19. *Cont.*

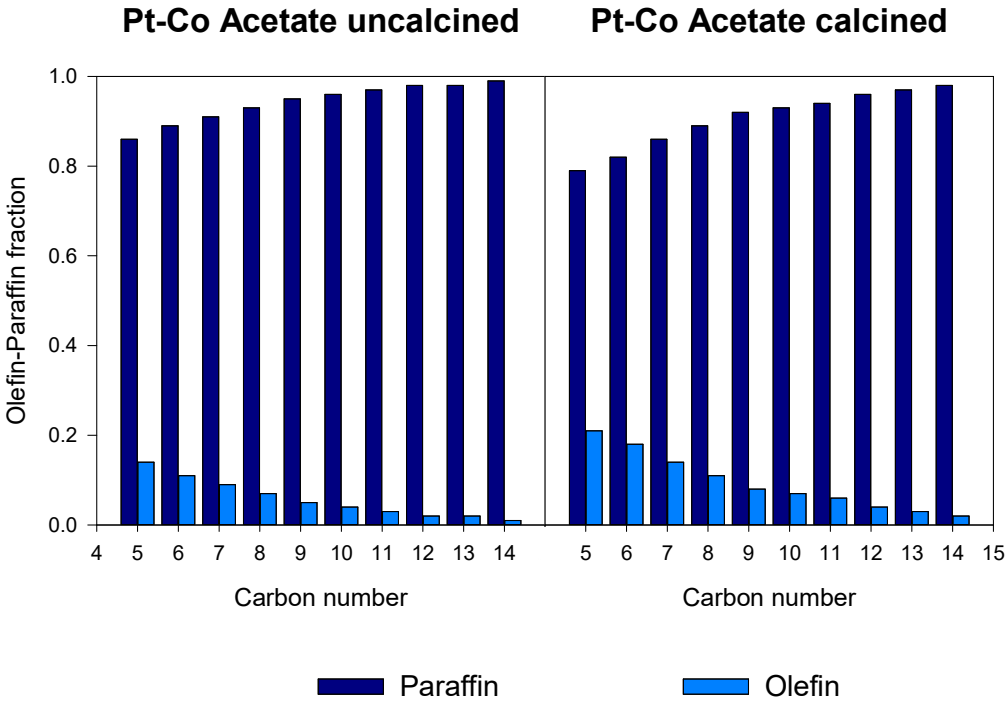

Figure 19. Fraction of olefins and paraffins for C_5–C_{14} hydrocarbons (T = 220 °C, P= 20 atm, H_2/CO = 2 mol/mol, SV = 6 slph/g_{cat}).

Interestingly, the Pt-Co/silica catalyst derived from cobalt acetate and prepared by air calcination/H_2 reduction performed significantly better (C_{5+} of 65.9% versus 58.7%; α-value of 0.766 versus 0.693; and higher olefin fractions) than the catalyst prepared by direct reduction, which is opposite to what we observed with the Pt-Co/silica prepared from cobalt nitrate. This improvement in selectivity with the air calcination of cobalt acetate prior to H_2 reduction strongly suggests that the removal of residual carbon from the catalyst, present as cobalt carbide, is an issue. In the future, we will strive to improve the selectivity of this catalyst further by carrying out oxidation-reduction cycles, as it is well known that cobalt carbide significantly increases light gas selectivity and suppresses activity [44].

4. Conclusions

The strength of the interaction between Co species and the support depends significantly on the type of Co precursor used. Using cobalt chloride as a precursor results in a very large average cobalt particle size due to the weak interactions between cobalt species and silica, resulting in agglomeration and loss of the cobalt active site density following activation in H_2. In this respect, cobalt chloride is an even worse compound than the traditional one, Co_3O_4, derived from the air calcination of cobalt nitrate, the latter of which also results in large Co^0 particles (e.g., 24–52 nm) on silica following activation in H_2.

On the other hand, cobalt acetate shows promise. In this investigation, the best catalyst in terms of activity on a per gram of catalyst basis was the H_2-activated, air-calcined Pt-promoted Co/SiO_2 catalyst derived from cobalt acetate, as well as the same catalyst but prepared from the direct reduction of cobalt acetate. The H_2-TPR profiles reveal that the calcined and uncalcined Pt-Co/silica catalysts derived from Co acetate catalyst follow completely different rates of reduction during activation, not only in comparison to each other but also compared to the counterpart catalysts prepared from Co nitrate (where the trend is the opposite). In the case of the Pt-Co/silica catalysts derived from Co acetate, direct reduction was too facile, resulting in relatively larger-than-ideal Co particles (~19.5 nm) and an active site density of 21.4 micromoles of H_2 desorbed per gram of catalyst, while air calcination and reduction led to strong interactions, an ideal Co particle size (7.8 nm), and

a higher active site density of 49.5 micromoles H_2 desorbed per gram of catalyst. This site density was higher than that of our best cobalt/silica catalyst to date, Pt-Co/SiO_2 prepared from the direct H_2 reduction of cobalt nitrate (active site density of 39.2 micromoles H_2 desorbed per gram of catalyst and an average diameter of 8.9 nm) and far higher than that of the conventional air-calcined/H_2-reduced Co/SiO_2 and Pt-Co/SiO_2 catalysts (10.8 and 19.3 micromoles per gram of catalyst, respectively) from cobalt nitrate.

The XANES and EXAFS spectra of the uncalcined catalyst revealed the existence of a fraction of cobalt carbide after reducing in H_2 up to 560 °C; this carbide is detrimental to both activity and selectivity. Despite having different active site densities, both the Pt-Co/silica catalysts derived from cobalt acetate had a similar CO conversion, which was ~20% higher (relative basis) than that of the conventional air-calcined Pt-promoted catalyst prepared from cobalt nitrate. A fraction of cobalt in Pt-Co/silica catalysts derived from cobalt acetate and with air calcination/reduction likely consisted of tiny Co crystallites due to the reduction of Co species in strong interaction with the silica support. Following air calcination, the TPR profiles in the unpromoted catalysts were significantly broadened, suggesting strong interactions between tiny cobalt oxide species and the silica support. It is known that Co particles below 2–4 nm are susceptible to oxidation at the onset of FTS due to indigenous H_2O; however, residual cobalt carbide present in the catalyst can also hinder activity. Both Pt-Co/silica catalysts derived from cobalt acetate had a CO conversion that was three times higher than that of the conventional Pt-Co/silica catalyst prepared from the air calcination of cobalt nitrate followed by H_2 reduction. However, the catalysts had 75% of the initial CO conversion of our best catalyst to date (in terms of activity), which is the Pt-Co/silica catalyst derived from the direct reduction of cobalt nitrate. Due to the retention of some carbon in the catalyst resulting in excessive hydrogenation/termination, the Pt-Co/SiO_2 catalysts derived from cobalt acetate had higher C_1-C_4 selectivity (32.2% air-calcined and 38.7% uncalcined) relative to the unpromoted and Pt-promoted catalysts prepared from cobalt nitrate (17.5–18.6%). In addition, the chain growth probability (α) values were lower for the Pt-Co/SiO_2 catalysts derived from cobalt acetate (0.766 air-calcined and 0.693 uncalcined) relative to the catalysts derived from cobalt nitrate (0.789–0.792). Olefin/paraffin ratios trended with the α-values. Of the Pt-Co/SiO_2 catalysts derived from cobalt acetate, the air-calcined catalysts had a better selectivity, suggesting that further improvements might be possible with oxidation–reduction cycles, and this aspect will be investigated in the future. Due to the lower costs associated with cobalt acetate, this precursor is of significant interest.

Author Contributions: Conceptualization, investigation, visualization, resources, formal analysis, supervision, writing, G.J. Investigation, visualization, formal analysis, supervision, writing, M.M. (Mohammad Mehrbod). Investigation, visualization, formal analysis, conceptualization, writing, M.M. (Michela Martinelli). Investigation, visualization, formal analysis, writing. C.D.W. Investigation, supervision, resources, D.C.C. Investigation, visualization, data curation, resources, supervision, A.J.K. All authors have read and agreed to the published version of the manuscript.

Funding: Caleb D. Watson would like to acknowledge support from the Undergraduate NSF Research Program, supported by the National Science Foundation through grant award #1832388.

Acknowledgments: The authors declare no conflict of interest.

Conflicts of Interest: Argonne's research was supported in part by the U.S. Department of Energy (DOE), Office of Fossil Energy, National Energy Technology Laboratory (NETL). Advanced photon source was supported by the U.S. Department of Energy, Office of Science, Office of Basic Energy Sciences, under contract number DE-AC02-06CH11357. MRCAT operations are supported by the Department of Energy and the MRCAT member institutions. CAER research was supported by the Commonwealth of Kentucky. Caleb D. Watson would like to acknowledge funding from a UTSA College of Engineering Scholarship. Gary Jacobs would like to thank UTSA and the State of Texas for financial support through startup funds.

References

1. Schaub, G.; Rohde, M.; Subiranas, A.M. Fischer-Tropsch synthesis. In *Development and Perspectives, Proceedings of the DGMK/SCI-Conference "Synthesis Gas Chemistry", Dresden, Germany, 4–6 October 2006*; Ernst, S., Jess, A., Nees, F., Perego, C., Rupp, M., Santacesaria, E., Eds.; German Society for Petroleum and Coal Science and Technology: Hamburg, Germany, 2006; pp. 75–84.
2. Espinoza, R.L.; Visagie, J.L.; van Berge, P.J.; Bolder, F.H. Catalysts. U.S. Patent 5,733,839, 31 March 1998.
3. Iglesia, E. Design, synthesis, and use of cobalt-based Fischer-Tropsch synthesis catalysts. *Appl. Catal. A Gen.* **1997**, *161*, 59–78. [CrossRef]
4. Jacobs, G.; Das, T.K.; Zhang, Y.; Li, J.; Racoillet, G.; Davis, B.H. Fischer-Tropsch synthesis: Support, loading, and promoter effects on the reducibility of cobalt catalysts. *Appl. Catal. A Gen.* **2002**, *233*, 263–281. [CrossRef]
5. Wang, W.-J.; Chen, Y.-W. Influence of metal loading on the reducibility and hydro-genation activity of cobalt/alumina catalysts. *Appl. Catal.* **1991**, *77*, 223–233. [CrossRef]
6. Diehl, F.; Khodakov, A.Y. Promotion of cobalt Fischer-Tropsch catalysts with noble metals: A review. *Oil Gas. Sci. Technol. Rev. l'IFP* **2009**, *64*, 11–24. [CrossRef]
7. Vada, S.; Hoff, A.; Adnanes, E.; Schanke, D.; Holmen, A. Fischer-Tropsch synthesis on supported cobalt catalysts promoted by platinum and rhenium. *Top. Catal.* **1995**, *2*, 155–162. [CrossRef]
8. Cook, K.M.; Poudyal, S.; Miller, J.T.; Bartholomew, C.H.; Hecker, W.C. Reducibility of alumina-supported cobalt Fischer-Tropsch catalysts: Effects of noble metal type, distribution, retention, chemical state, bonding, and influence on cobalt crystallite size. *Appl. Catal. A Gen.* **2012**, *449*, 69–80. [CrossRef]
9. Jacobs, G.; Chaney, J.A.; Patterson, P.M.; Das, T.K.; Davis, B.H. Fischer-Tropsch synthesis: Study of the promotion of Re on the reduction property of Co/Al_2O_3 catalysts by in situ EXAFS/XANES of Co K and Re L_{III} edges and XPS. *Appl. Catal. A Gen.* **2004**, *264*, 203–212. [CrossRef]
10. Ronning, M.; Nicholson, D.G.; Holmen, A. In situ EXAFS study of the bimetallic inter-action in a rhenium-promoted alumina-supported cobalt Fischer-Tropsch catalyst. *Catal. Lett.* **2001**, *72*, 141–146. [CrossRef]
11. Guczi, L.; Bazin, D.; Kovacs, I.; Borko, L.; Schay, Z.; Lynch, J.; Parent, P.; Lafon, C.; Stefler, G.; Koppany, Z.; et al. Structure of Pt-Co/Al_2O_3 and Pt-Co/NaY bimetallic catalysts: Characterization by in situ EXAFS, TPR, XPS and by activity in CO Hydrogenation. *Top. Catal.* **2002**, *20*, 129–139. [CrossRef]
12. Jacobs, G.; Chaney, J.A.; Patterson, P.M.; Das, T.K.; Maillot, J.C.; Davis, B.H. Fischer-Tropsch synthesis: Study of the promotion of Pt on the reduction property of Co/Al_2O_3 catalysts by in situ EXAFS of Co K and Pt L_{III} edges and XPS. *J. Synch. Rad.* **2004**, *11*, 414–422. [CrossRef] [PubMed]
13. Iglesia, E.; Soled, S.L.; Fiato, R.A.; Via, G.H. Bimetallic synergy in cobalt-ruthenium Fischer-Tropsch synthesis catalysts. *J. Catal.* **1993**, *143*, 345–368. [CrossRef]
14. Lok, C.M.; Shannon, M.D.; Casci, J.L. Imaging promoter atoms in cobalt Fischer-Tropsch catalysts using SuperSTEM microscopy. *Stud. Surf. Sci. Catal.* **2006**, *172*, 257–260.
15. Ma, W.; Jacobs, G.; Qian, D.; Ji, Y.; Klettlinger, J.L.S.; Hopps, S.D.; Davis, B.H. Fischer-Tropsch synthesis: Synergistic effect of hybrid Pt-Cd additives on a 15%Co/Al_2O_3 catalyst. *Appl. Catal. A Gen.* **2020**, *600*, 117610. [CrossRef]
16. Van Steen, E.; Claeys, M.; Dry, M.E.; van de Loosdrecht, J.; Viljoen, E.L.; Visagie, J.L. Stability of nanocrystals: Thermodynamic analysis of oxidation and re-reduction of cobalt in water/hydrogen mixtures. *J. Phys. Chem. B* **2005**, *109*, 3575–3577. [CrossRef]
17. Loegdberg, S.; Boutonnet, M.; Walmsley, J.C.; Jaras, S.; Holmen, A.; Blekkan, E.A. Effect of water on the space-time yield of different supported cobalt catalysts during Fiscer-Tropsch synthesis. *Appl. Catal. A Gen.* **2011**, *393*, 109–121. [CrossRef]
18. Jacobs, G.; Das, T.K.; Patterson, P.M.; Li, J.; Sanchez, L.; Davis, B.H. Fischer-Tropsch synthesis: XAFS studies of the effect of water on a Pt-promoted Co/Al_2O_3 catalyst. *Appl. Catal. A Gen.* **2003**, *247*, 335–343. [CrossRef]
19. Hughes, N.A.; Gloriot, V.; Smiley, D.D.; Jacobs, G.; Pendyala, V.R.R.; Graham, U.M.; Ma, W.; Gnanamani, M.K.; Shafer, W.D.; Maclennan, A.; et al. Fischer-Tropsch synthesis: Comparisons of Al_2O_3 and TiO_2 supported Co catalysts prepared by aqueous impregnation and CVD methods. In *Fischer-Tropsch Synthesis, Catalysts and Catalysis: Advances and Applications*; Davis, B.H., Occelli, M.L., Eds.; CRC Press: Boca Raton, FL, USA; Taylor & Francis Group: Abingdon, UK, 2016; pp. 85–106, Chapter 6.
20. Jermwongratanachai, T.; Jacobs, G.; Shafer, W.D.; Ma, W.; Pendyala, V.R.R.; Davis, B.H.; Kitiyanan, B.; Khalid, S.; Cronauer, D.C.; Kropf, A.J.; et al. Fischer-Tropsch synthesis: Oxidation of a fraction of cobalt crystallites in research catalysts at the onset of FT at partial pressures mimicking 50% CO conversion. *Top. Catal.* **2014**, *57*, 479–490. [CrossRef]
21. Hou, C.; Xia, G.; Sun, X.; Wu, Y.; Jin, C.; Yan, Z.; Li, M.; Hu, Z.; Nie, H.; Li, D. Thermodynamics of oxidation of an alumina-supported cobalt catalyst by water in F-T synthesis. *Catal. Today* **2016**, *264*, 91–97. [CrossRef]
22. Bambal, A.S.; Kugler, E.L.; Gardner, T.H.; Dadyburjor, D.B. Effect of Surface Modification by Chelating Agents on Fischer−Tropsch Performance of Co/SiO_2 Catalysts. *Ind. Eng. Chem. Res.* **2013**, *52*, 16675–16688. [CrossRef]
23. Cronauer, D.C.; Elam, J.W.; Kropf, A.J.; Marshall, C.L.; Gao, P.; Hopps, S.; Jacobs, G.; Davis, B.H. Fischer-Tropsch synthesis: Preconditioning effects upon Co-containing promoted and unpromoted catalysts. *Catal. Lett.* **2012**, *142*, 698–713. [CrossRef]
24. Bae, J.W.; Kim, S.-M.; Kang, S.-H.; Chary, K.V.R.; Lee, Y.-J.; Kim, H.-J.; Jun, K.-W. Effect of support and cobalt precursors on the activity of $Co/AlPO_4$ catalysts in Fischer-Tropsch synthesis. *J. Mol. Catal. A Chem.* **2009**, *311*, 7–16. [CrossRef]
25. Panpranot, J.; Kaewkun, S.; Praserthdam, P.; Goodwin, J.G. Effect of cobalt precursors on the dispersion of cobalt on MCM-41. *Catal. Lett.* **2003**, *91*, 95–102. [CrossRef]

26. Sun, S.; Tsubaki, N.; Fujimoto, K. The reaction performances and characterization of Fischer-Tropsch synthesis Co/SiO_2 catalysts prepared from mixed cobalt salts. *Appl. Catal. A Gen.* **2000**, *202*, 121–131. [CrossRef]
27. Tsubaki, N.; Sun, S.; Fujimoto, K. Different Functions of the Noble Metals Added to Cobalt Catalysts for Fischer-Tropsch Synthesis. *J. Catal.* **2001**, *199*, 236–246. [CrossRef]
28. Girardon, J.-S.; Lermontov, A.S.; Gengembre, L.; Chernavskii, P.A.; Griboval-Constant, A.; Khodakov, A.Y. Effect of cobalt precursor and pretreatment conditions on the structure and catalytic performance of cobalt silica-supported Fischer-Tropsch catalysts. *J. Catal.* **2005**, *230*, 339–352. [CrossRef]
29. Li, J.; Zhan, X.; Zhang, Y.; Jacobs, G.; Das, T.K.; Davis, B.H. Fischer-Tropsch synthesis: Effect of water on the deactivation of Pt promoted Co/Al_2O_3 catalysts. *Appl. Catal. A Gen.* **2002**, *228*, 203–212. [CrossRef]
30. Davis, B.H.; Iglesia, E. *Technology Development for Iron and Cobalt Fischer-Tropsch Catalysts*; National Energy Technology Laboratory (NETL): Pittsburgh, PA, USA, 2002.
31. Wigzell, F.A.; Jackson, S.D. The genesis of supported cobalt catalysts. *Appl. Petrochem. Res.* **2017**, *7*, 9–21. [CrossRef]
32. Martinelli, M.; Mehrbod, M.; Dawson, C.; Davis, B.H.; Lietti, L.; Cronauer, D.C.; Kropf, A.J.; Marshall, C.L.; Jacobs, G. Fischer-Tropsch synthesis: Foregoing calcination and utilizing reduction promoters leads to improved conversion and selectivity with Co/silica. *Appl. Catal. A Gen.* **2018**, *559*, 153–166. [CrossRef]
33. Mehrbod, M.; Martinelli, M.; Castro, J.D.; Alhraki, N.; Cronauer, D.C.; Kropf, A.J.; Marshall, C.L.; Jacobs, G. Fischer-Tropsch synthesis: Direct cobalt nitrate reduction of promoted Co/Al_2O_3 catalysts. *Catal. Today* **2021**, *369*, 129–143. [CrossRef]
34. Mehrbod, M.; Martinelli, M.; Martino, A.G.; Cronauer, D.C.; Kropf, A.J.; Marshall, C.L.; Jacobs, G. Fischer-Tropsch synthesis: Direct cobalt nitrate reduction of promoted Co/TiO_2 catalysts. *Fuel* **2019**, *245*, 488–504. [CrossRef]
35. Millipore-Sigma, Chemical Supplier. Available online: https://www.sigmaaldrich.com/united-states.html (accessed on 21 March 2021).
36. *The MAK-Collection Part. I: MAK Value Documentations*; DFG, Deutsche Forschungsgemeinschaft; Wiley-VCH Verlag GmbH & Co. KgaA: Weinheim, Germany, 2007; Volume 23, ISBN 978-3-527-31595-6.
37. Krumm, S. The Erlangen geological and mineralogical software collection. *Comput. Geosci.* **1999**, *25*, 489–499. [CrossRef]
38. Jacoby, M. X-ray Absorption Spectroscopy. *Chem. Engin. News Arch.* **2001**, *79*, 33–38. [CrossRef]
39. Ressler, T. WinXAS: A Program for X-ray Absorption Spectroscopy Data Analysis under MS-Windows. *J. Synchrot. Radiat.* **1998**, *5*, 118–122. [CrossRef]
40. Jacobs, G.; Ji, Y.; Davis, B.H.; Cronauer, D.C.; Kropf, A.J.; Marshall, C.L. Fischer-Tropsch synthesis: Temperature programmed EXAFS/XANES investigation of the influence of support type, cobalt loading, and noble metal promoter addition to the reduction behavior of cobalt oxide particles. *Appl. Catal. A Gen.* **2007**, *333*, 177–191. [CrossRef]
41. Ravel, B. ATOMS: Crystallography for the X-ray absorption spectroscopist. *J. Synchrot. Radiat* **2001**, *8*, 314–316. [CrossRef] [PubMed]
42. Newville, M.; Ravel, B.; Haskel, D.; Rehr, J.J.; Stern, E.A.; Yacoby, Y. Analysis of multiple-scattering XAFS data using theoretical standards. *Physical B* **1995**, *208–209*, 154–156. [CrossRef]
43. Mohamed, M.; Halawy, S.; Ebrahim, M. The non-isothermal decomposition of cobalt acetate tetrahydrate: A kinetic and thermodynamic study. *J. Therm. Anal. Calor.* **1994**, *41*, 387–404. [CrossRef]
44. Mohandas, J.C.; Gnanamani, M.K.; Jacobs, G.; Ma, W.; Ji, Y.; Khalid, S.; Davis, B.H. Fischer-Tropsch synthesis: Synthesis, characterization, and reaction testing investigation of cobalt carbide. *ACS Catal.* **2011**, *1*, 1581–1588. [CrossRef]